RSC Advances

PAPER

View Article Online
View Journal | View Issue



Cite this: *RSC Adv.*, 2023, **13**, 35853

# Rationale design and synthesis of new apoptotic thiadiazole derivatives targeting VEGFR-2: computational and *in vitro* studies†

Walid E. Elgammal,[a] Hazem Elkady,[b] Hazem A. Mahdy,[b] Dalal Z. Husein,[c] Aisha A. Alsfouk,[d] Bshra A. Alsfouk,[d] Ibrahim M. Ibrahim,[e] Eslam B. Elkaeed,*[f] Ahmed M. Metwaly *[gh] and Ibrahim H. Eissa *[b]

This work presents the synthesis and *in vitro*, and *in silico* analyses of new thiadiazole derivatives that are designed to mimic the pharmacophoric characteristics of vascular endothelial growth factor receptor-2 (VEGFR-2) inhibitors. A comprehensive evaluation of the inhibitory properties of the synthesized thiadiazole derivatives against the cancer cell lines MCF-7 and HepG2 identified several auspicious candidates. Among them, compound **14** showed remarkably low $IC_{50}$ values of 0.04 μM and 0.18 μM against MCF-7 and HepG2, respectively. VEGFR-2 inhibitory evaluation of compound **14** revealed a promising $IC_{50}$ value in the nanomolar range (103 nM). Further examination of the cell cycle revealed that compound **14** has the ability to stop the progression of the cell cycle in MCF-7 cells *via* G0–G1 phase arrest. Interestingly, compound **14** also demonstrated a noteworthy pro-apoptotic effect in MCF-7 cells, with notable increases in early apoptosis (16.53%) and late apoptosis (29.57%), along with a slight increase in the population of necrotic cells (5.95%). Furthermore, compound **14** showed a significant drop in MCF-7 cells' ability to migrate and heal wounds. Additionally, compound **14** promoted apoptosis by boosting BAX (6-fold) while lowering Bcl-2 (6.2-fold). The binding affinities of the synthesized candidates to their target (VEGFR-2) were confirmed by computational investigations, including molecular docking, principal component analysis of trajectories (PCAT), and molecular dynamics (MD) simulations. Additionally, compound **14**'s stability and reactivity were investigated using density functional theory (DFT). These thorough results highlight compound **14**'s potential as a lead contender for additional research in the creation of anticancer drugs that target VEGFR-2. This work establishes a foundation for promising thiadiazole derivatives for future therapeutic developments in anticancer- and angiogenesis-related scientific fields.

Received 5th November 2023
Accepted 24th November 2023

DOI: 10.1039/d3ra07562a

rsc.li/rsc-advances



## 1. Introduction

In 2021, the International Agency for Research on Cancer (IARC), a division of the World Health Organization (WHO), reported that there were 19 292 789 new cases of cancer worldwide in 2020, resulting in 9 958 133 fatalities.[1] These numbers underscore how serious and widespread cancer is, underlining the crucial need for ongoing, thorough scientific exploration to find new ways to treat it. This effort is vital for advancing our understanding and developing more effective methods in our fight against this tough disease.

Vascular endothelial growth factor receptor 2 (VEGFR-2) is a transmembrane receptor primarily found on the surface of endothelial cells, which form the inner lining of blood vessels. In the context of cancer, VEGFR-2 is of particular interest because it is overexpressed in many types of tumor.[2,3] This overexpression leads to increased signaling through the VEGF pathway, which promotes the growth of new blood vessels around the tumor, a phenomenon known as

[a]*Department of Chemistry, Faculty of Science, Al-Azhar University, Nasr City, Cairo, Egypt*

[b]*Pharmaceutical Medicinal Chemistry & Drug Design Department, Faculty of Pharmacy (Boys), Al-Azhar University, Cairo 11884, Egypt*

[c]*Chemistry Department, Faculty of Science, New Valley University, El-Kharja 72511, Egypt*

[d]*Department of Pharmaceutical Sciences, College of Pharmacy, Princess Nourah bint Abdulrahman University, P.O. Box 84428, Riyadh 11671, Saudi Arabia*

[e]*Biophysics Department, Faculty of Science, Cairo University, Giza 12613, Egypt. E-mail: Ibrahim_mohamed@cu.edu.eg*

[f]*Department of Pharmaceutical Sciences, College of Pharmacy, AlMaarefa University, Riyadh 13713, Saudi Arabia. E-mail: ekaeed@um.edu.sa*

[g]*Pharmacognosy and Medicinal Plants Department, Faculty of Pharmacy (Boys), Al-Azhar University, Cairo 11884, Egypt. E-mail: ametwaly@azhar.edu.eg*

[h]*Biopharmaceutical Products Research Department, Genetic Engineering and Biotechnology Research Institute, City of Scientific Research and Technological Applications (SRTA-City), Alexandria, Egypt*

† Electronic supplementary information (ESI) available. See DOI: https://doi.org/10.1039/d3ra07562a

angiogenesis,[4] which is a crucial process for tumor survival, growth, and metastasis.[5,6] Furthermore, recent research has observed a correlation between heightened expression of VEGFR-2 and heightened resistance to cancer drugs, amplified angiogenesis,[7] and diminished apoptosis.[8] Consequently, targeting VEGFR-2 has emerged as a promising therapeutic strategy.

VEGFR-2 inhibitors are a class of drugs designed to block the activity of this receptor. The inhibition of VEGFR-2 will disrupt the angiogenic process and starve the tumor of vital resources, impeding its ability to grow and spread.[9] Unfortunately, inhibitors targeting VEGFR-2 have been linked to severe adverse effects, such as elevated blood pressure,[10] proteinuria,[11] instances of bleeding,[12] germline polymorphisms,[13] and reversible posterior leukoencephalopathy syndrome.[10,14] These adverse effects underscore the pressing need for research into new safer alternatives. The development of novel VEGFR-2 inhibitors holds the potential to enhance treatment effectiveness and overall well-being for patients, thereby advancing the quality of cancer care.

Computational chemistry revolutionized anticancer research by enabling the precise design of targeted inhibitors.[15] This technology employs computational power to design molecules tailored to interact specifically with specific receptors in the cancer cells.[16,17] It also predicts the stability of these designed molecules, streamlining drug development and the optimization of lead compounds.[18] Additionally, it anticipates the binding affinity of these molecules with the targeted receptors, expediting screening and enhancing efficacy against cancer cells.[19] Furthermore, this approach shows promise in minimizing side effects associated with traditional chemotherapy through the precise targeting of cancer-specific pathways.[20,21] This selectivity could revolutionize cancer treatment, providing therapies that are not only more potent against the disease but also safer for patients.[22,23]

Computational chemistry encompasses several approaches, such as design,[24] docking,[25] and prediction of ADMET (absorption, distribution, metabolism, excretion, and toxicity),[26] as well as DFT (density functional theory).[27] These tools have been utilized to identify compounds that show

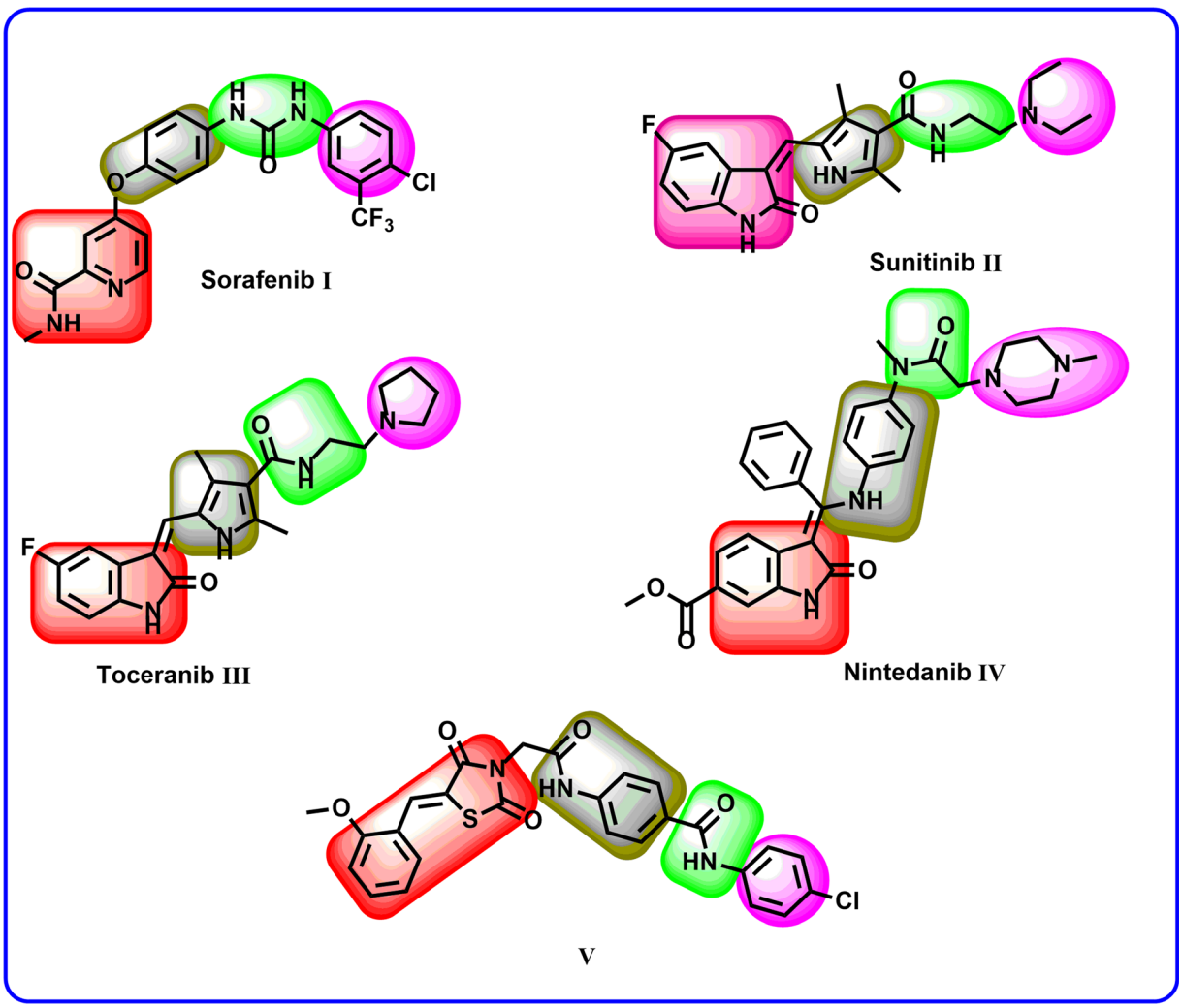


Fig. 1 Some reported VEGFR-2 inhibitors showing the essential pharmacophoric features.

potential for effective anticancer activity in numerous research studies.[28–31] Our laboratory has employed computational chemistry to present new VEGFR-2 inhibitors, including quinolones,[32] isatins,[33] theobromines,[34–38] benzoxazoles,[39,40] nicotinamides,[41,42] thiazolidines,[43] pyridines,[44] naphthalenes,[45] and indoles.[46] This manuscript introduces novel apoptotic thiadiazole analogues, which were synthesized for the first time and exhibited promising anticancer properties *in silico* and *in vitro*.

## 2. Rationale

The clinically used VEGFR-2 inhibitors and those under investigation are reported to have four pharmacophoric features for good binding with their biological target. The reported features are a hetero-aromatic head, a linker group, a pharmacophore group, and a hydrophobic tail[47–49] (Fig. 1). The different regions of the active site are the hinge, the gatekeeper, the DFG motif, and the allosteric region. The pharmacophore group is the most important one. It should have at least one hydrogen bond (H-bond) donor and one H-bond acceptor atom to form essential hydrogen bonds with Asp1044 and Glu883 in the DFG motif region. Drug discovery efforts have provided many FDA-approved VEGFR-2 inhibitors, such as sorafenib **I**,[50] sunitinib **II**,[51] toceranib **III**,[52] and nintedanib **IV**.[53] As shown in Fig. 1, the reported VEGFR-2 inhibitors share the same pharmacophoric features.

Recently, our team introduced compound **V** (ref. 54) as a potent VEGFR-2 inhibitor. This compound is a (*Z*)-5-benzylidenethiazolidine-2,4-dione derivative and it exhibited a high ability to inhibit VEGFR-2 ($IC_{50}$ = 0.081 μM) and stop the growth of three different cancer cell types (HT-29, A-549, and HCT-116). In addition, compound **V** exhibited a remarkable apoptotic effect in HT-29 cancer cells. Furthermore, it increased the levels of BAX, caspase-8, and caspase-9 and decreased the level of Bcl-2 in the same cells. Computational studies revealed the high potential of compound **V** to bind with its prospective target (VEGFR-2) with extended stability. The obtained results suggested compound **V** as a lead compound to guide future attempts to develop new drugs.

In the current work, compound **V** was used as a lead compound for further modifications, hoping to obtain more efficient VEGFR-2 inhibitors. First, the (*Z*)-5-(2-methoxy benzylidene)thiazolidine-2,4-dione moiety (hetero cyclic head) of compound **V** was replaced by substituted 3-phenyl-2,3-dihydro-1,3,4-thiadiazole moieties. In this modification, the five-membered ring (thiazolidine-2,4-dione) was replaced by an equivalent five-membered ring (2,3-dihydro-1,3,4-thiadiazole). In addition, the attached phenyl ring was unchanged while the one-carbon bridge was removed. The second modification involved the replacement of the *N*-phenylacetamide (linker) moiety with (1-phenylethylidene)hydrazine. In this modification, the length of the linker moiety was not changed. Regarding the pharmacophore (amide) moiety of the lead compound, it was kept as it is to match the pharmacophore moiety of sunitinib **II**,[51] toceranib **III**,[52] and nintedanib **IV**.[53] Finally, the 4-chlorophenyl (hydrophobic tail) moiety of the lead compound was replaced by methyl and different substituted phenyl rings (Fig. 2).

## 3. Results and discussion

### 3.1. Chemistry

This article focuses on the synthesis of a series of innovative thiadiazole derivatives. We obtained the novel targeted compounds through the synthetic pathways illustrated in Schemes 1–3. Briefly, precursor **2** (ref. 55) was synthesized by chlorination of acetylacetone with sulfuryl chloride in anhydrous diethyl ether in an ice/NaCl bath with stirring. In the next step, compound **2** was coupled with appropriate benzene diazonium chloride **4** [prepared from substituted aniline derivatives **3a**, **3b** and a solution of sodium nitrite in the presence of diluted hydrochloric acid in an ice bath] to afford corresponding hydrazonoyl chlorides **5a** and **5b**.[56] The key intermediate **9** was obtained by first reacting hydrazine hydrate with carbon disulfide in isopropyl alcohol and potassium hydroxide, leading to the formation of intermediate **8**. This intermediate was then subjected to methylation using iodomethane, resulting in the formation of reagent **9**,[57] as presented in Scheme 1.

As shown in Scheme 2, compound **12** (ref. 58) was prepared *via* acetylation of 4-aminoacetophenone **10** with acetic anhydride under stirring at ambient room temperature. Then, compound **12** was heated under reflux with methyl hydrazinecarbodithioate **9** in absolute ethanol to provide methyl (*E*)-2-(1-(4-acetamidophenyl)ethylidene)hydrazine-1-carbodithioate **13**. Treatment of compound **13** with a hydrazonoyl chloride derivative **5a** in ethanol in the presence of triethylamine as a catalyst under refluxing temperature afforded the target thiadiazole derivative **14**.

In a similar vein, the reaction of 4-aminoacetophenone **10** with benzoyl chloride derivatives **15a–c** was carried out in the presence of triethylamine as a catalyst and DMF as a solvent. This reaction produced the derivatives **16a** and **16b**, which then reacted with hydrazinecarbodithioate **9** in boiling ethanol to form compounds **17a–c**. Afterward, compounds **17a–c** were allowed to react with hydrazonoyl chloride derivatives **5a** or **5b** in the presence of ethanol and TEA under heating, resulting in the formation of the respective 1,3,4-thiadiazole derivatives (**18a–f**) in good purity/yield, as demonstrated in Scheme 3.

The mechanism outlined in Fig. 3 seems likely to be responsible for the formation of compound **14**, *via* the reaction of **13** with **5a**. As soon as thiohydrazonate **20** is formed, it undergoes intermolecular cyclization to form intermediate **21**, or through 1,3-dipolar cycloaddition of nitrileimine **19a** or **19b** [prepared *in situ* from **5a** and **5b**, respectively, with triethylamine] to the C=S double bond of **13**. During the elimination of the alkanethiol ($CH_3SH\uparrow$), compound **21** was converted to compound **14**. In a similar way, combining **17a–c** with **5a** and **5b** resulted in the formation of 1,3,4-thiadiazoles **18a–f** with satisfactory yields (Fig. 1).

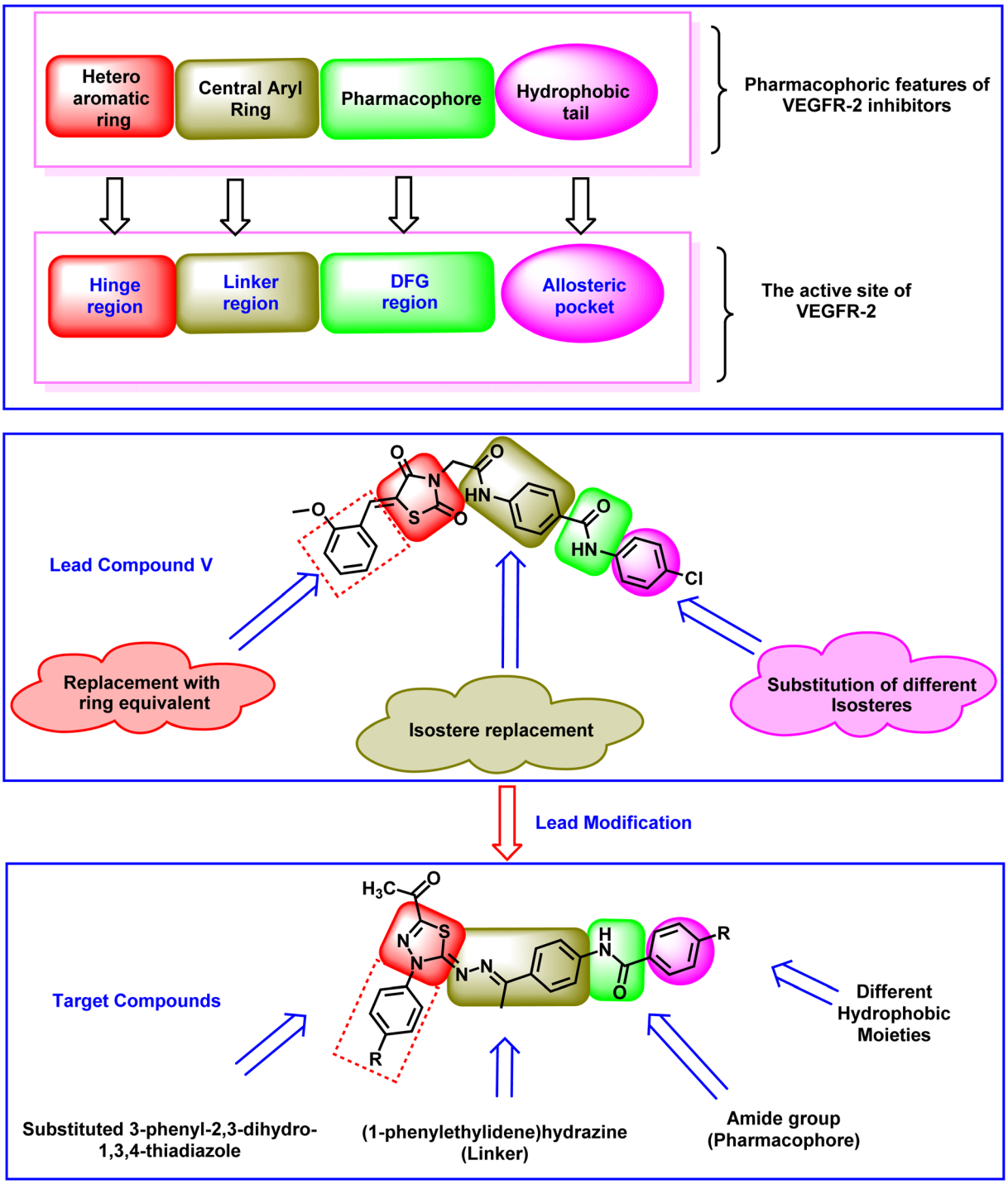


Fig. 2 The rationale of the presented design.

### 3.2. Biological evaluation

**3.2.1. *In vitro* cytotoxicity against MCF-7 and HepG2 cell lines.** The targeted thiadiazole analogues were tested *in vitro* for their anticancer activity against two distinct cell lines, MCF-7 and HepG2, since the overexpression of VEGFR-2 is well-reported to be associated with poor prognosis of breast and liver cancers.[2,59] Sorafenib was included in the experiments as a reference cytotoxic agent. The viability of the treated cells was determined using the MTT technique and the results are reported as $IC_{50}$ in Table 1. Investigation of the anti-proliferative activity towards the tested cell lines confirmed that the tested thiadiazole analogues exhibited moderate to excellent growth inhibitory influence ($IC_{50}$ ranged between 0.04 and 6.17 μM). Of special interest, the acetamide tail-bearing analog **14**, which displayed potent cytotoxic activity with $IC_{50}$ values of (0.04 and 0.18 μM) compared to sorafenib as a reference drug ($IC_{50}$ = 0.15

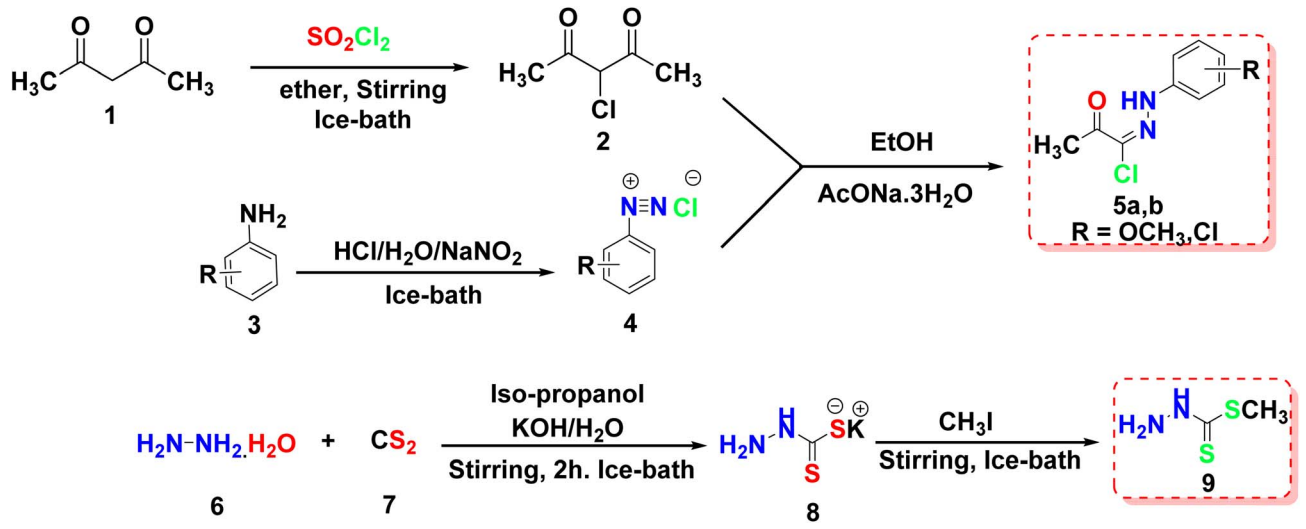


Scheme 1 Synthesis of the key intermediates **5a**, **5b**, and **9**.

and 0.14 μM) against MCF-7 and HepG2 cells, respectively. Likewise, the anti-proliferative activity for compounds **18a–f** bearing a benzamide moieties towards the two cancer cell lines varies significantly. The best results were exhibited by benzamide analogues (**18a**, **18c**, and **18e**) containing a 3-(4-methoxyphenyl)-2,3-dihydro-1,3,4-thiadiazole moiety.

In the context of the cytotoxicity of the benzamide counterparts **18a**, **18c**, and **18e**, it was found that unsubstituted benzamide analogue **18a** showed more significant cytotoxicity compared to the 4-chlorobenzamide **18c** or 4-methybenzamide **18e** ones.

Indeed, the incorporation of the 3-(4-chlorophenyl)-2,3-dihydro-1,3,4-thiadiazole moiety in **18b**, **18d**, and **10g** decreased the anti-proliferative action. Additionally, appending of unsubstituted benzamide **18b** is the most beneficial pattern within these counterparts **18b**, **18d**, and **10f**; replacement of the benzamide moiety with a 4-methybenzamide moiety (as in compound **18f**) led to a slightly decrease in the activity, while the incorporation of the 4-chlorobenzamide moiety (as in compound **18d**) led to a marked decrease in the activity.

**3.2.2. *In vitro* cytotoxicity against normal human lung cells (WI-38) and selectivity index.** Next, the safety of the most active cytotoxic compound **14** against a normal human cell line (WI-38) was examined to assess its selectivity for the two cancer cells. The obtained results (Table 2) revealed that compound **14** exhibited low cytotoxicity against normal cells with an $IC_{50}$ of $0.14 \pm 0$ μM in comparison to its toxicity against MCF-7)$IC_{50} = 0.04 \pm 0$ μM (and HepG2)$IC_{50} = 0.18 \pm 0$ μM) cancer cells. These results indicated that its cytotoxicity (selectivity index) against normal cells is about 28.57 and 1.28 times lower than the cytotoxicity against the two cancer cells, respectively.

**3.2.3. *In vitro* VEGFR-2 assay.** The most potent anti-proliferative derivative **14** was tested to evaluate its ability for VEGFR-2 kinase inhibition using sorafenib as a reference drug. The tested compound **14** displayed potent inhibitory activity with an $IC_{50}$ value of $0.103 \pm 0.004$ μg $mL^{-1}$, which was slightly less potent than sorafenib ($IC_{50} = 0.041 \pm 0.002$ μg $mL^{-1}$).

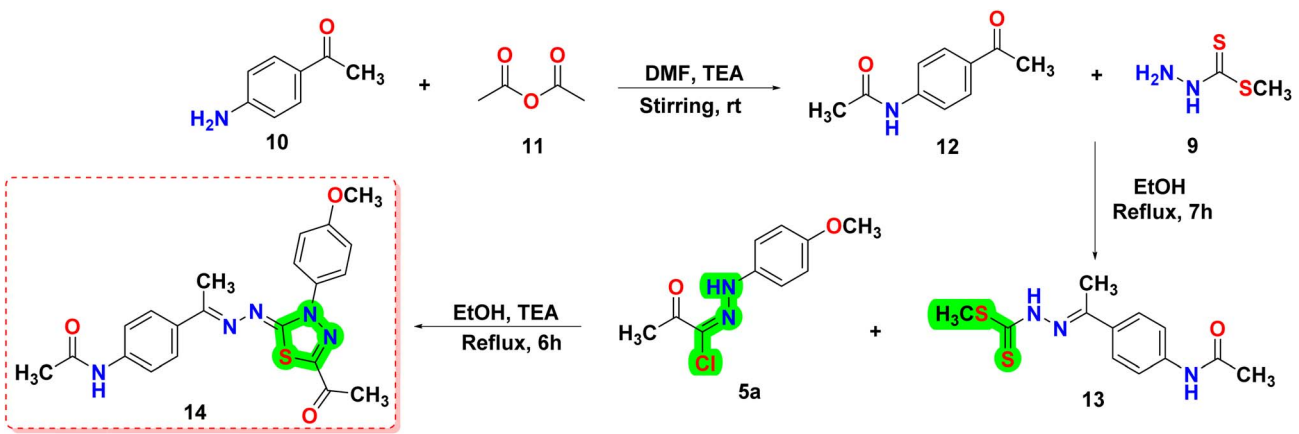


Scheme 2 Synthesis of the final compound **14**.

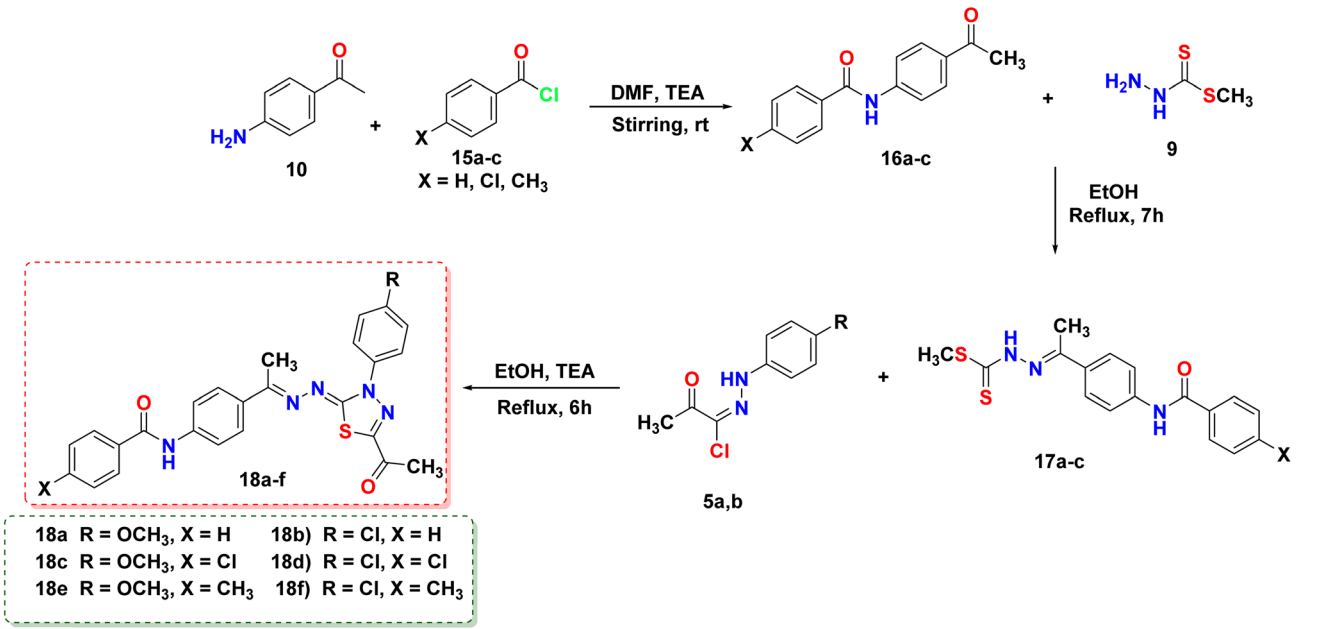


Scheme 3 Synthesis of the final compounds 18a–f.

### 3.2.4. Cellular mechanistic studies

*3.2.4.1. Cell cycle analysis.* Compound **14** showed potent cytotoxic and VEGFR-2 inhibition activities and was selected to explore its activity on the cell cycle distribution of MCF-7 cells. The MCF-7 cells were exposed to compound **14** (0.041 μM, equal to its anti-proliferative $IC_{50}$) for 72 hours, and cell cycle progression was monitored by flow cytometry; the results are reported in Table 3.

The obtained data revealed that compound **14** decreased the distribution in the S phase (22.27%) and the G2/M phase (9.3%) compared with the control (23.91 and 13.72%, respectively). In addition, the percentage of cell population increased at the G0–G1 phase by 1.09-fold more than the control. These findings revealed that compound **14** induced arrest of the cell cycle of the MCF-7 cells at the G0–G1 phase (Fig. 4).

*3.2.4.2. Apoptosis assay.* The MCF-7 cells were treated with compound **14** (0.04 μM for 72 h), and the apoptotic effect was

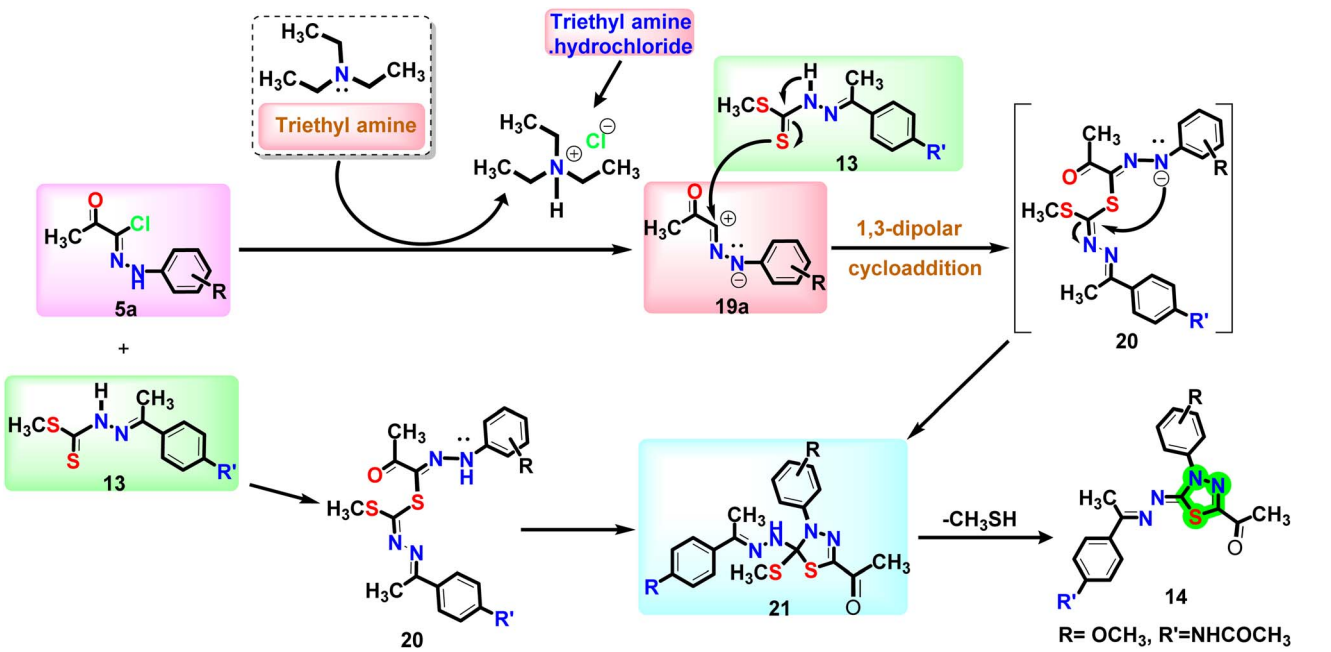


Fig. 3 Possible reaction mechanism for the formation of compounds 14 and 18a–f.

Table 1 *In vitro* anti-proliferative activities of the synthesized thiadiazole derivatives against MCF-7 and MCF-7 cell lines

| | *In vitro* cytotoxicity $IC_{50}$[a] (μM) | |
|---|---|---|
| Compound | MCF-7 | HepG2 |
| **14** | 0.04 ± 0.009 | 0.18 ± 0.006 |
| **18a** | 0.16 ± 0.017 | 0.80 ± 0.012 |
| **18b** | 0.22 ± 0.098 | 0.20 ± 0.011 |
| **18c** | 0.19 ± 0.014 | 0.16 ± 0.032 |
| **18d** | 5.00 ± 0.192 | 6.17 ± 0.019 |
| **18e** | 0.19 ± 0.045 | 0.21 ± 0.045 |
| **18f** | 0.44 ± 0.065 | 0.18 ± 0.018 |
| Sorafenib | 0.15 ± 0.013 | 0.14 ± 0.052 |

[a] Data are presented as mean of the $IC_{50}$ values from three different experiments.

Table 2 *In vitro* cytotoxicity of the thiadiazole derivative **14** against WI-38 cells and its selectivity index values for MCF-7 and HepG2 cell lines

| | | Selectivity index | |
|---|---|---|---|
| Compound | WI-38 $IC_{50}$[a] (μM) | MCF-7 | HepG2 |
| 14 | 0.14 ± 0 | 28.57 | 1.28 |

[a] Data are presented as mean of the $IC_{50}$ values from three different experiments.

Table 3 Effect of compound **14** on MCF-7 cell cycle progression

| | Cell cycle distribution (%) | | |
|---|---|---|---|
| Sample | G0–G1 | S | G2/M |
| Compound **14**-treated MCF-7 cells | 68.43 | 22.27 | 9.3 |
| MCF-7 cells | 62.37 | 23.91 | 13.72 |

assessed using the annexin V-FITC/PI assay. The results (Table 4) demonstrated that, compound **14** enhanced total apoptosis by 22-fold compared to the control (52.05% and 2.28%, respectively). Additionally, **14** increased the percentage of early apoptosis compared with the control MCF-7 cells (16.53% and 0.61%, respectively). Moreover, it increased the percentage of late apoptotic cells by 132-fold more than the control cells (from 0.24% to 29.57%). In addition, compound **14** enhanced the necrosis percentage four-fold more than the control. These details suggest that compound **14** can induce the apoptotic mechanism of programed cell death in the MCF-7 cell line (Fig. 5).

*3.2.4.3. BAX and BCl-2 analysis.* This investigation examined the effects of compound **14** at a concentration of 0.04 μM on the expression levels of well-known apoptotic markers, BAX and Bcl-2, in MCF-7 cells. The findings of this examination showed that compound **14** significantly boosted the level of the pro-apoptotic protein (BAX) by six-fold when compared to the control MCF-7 cells. Furthermore, compound **14** dramatically lowered levels of the anti-apoptotic protein Bcl-2 by 6.2-fold compared to the control MCF-7, as presented in Table 5.

*3.2.4.4. Cell migration and wound healing assay.* Cell migration is a pivotal step in cancer development and progression. Assessment of *in vitro* migration processes in cancer cell lines can be a crucial tool for studying new potential therapeutic anticancer drugs in order to understand cellular mechanistic pathways. The impact of compound **14** on the cell migration of MCF-7 cells was evaluated by using the *in vitro* scratch wound healing assay protocol.[60,61] This protocol involves the generation of a scratch on a monolayer of MCF-7 cancer cells, measuring the initial diameter, and checking the scratch's closure for both treated and untreated cells after 0 and 48 hours.

As shown in Table 6 and Fig. 6, the scratch width of the control MCF-7 cells was reduced by about 67.55% after 48 hours and appeared to be approximately closed, while the scratch width of the MCF-7 cells treated with compound **14** was only reduced by about 38.76% after 48 hours. This finding showed

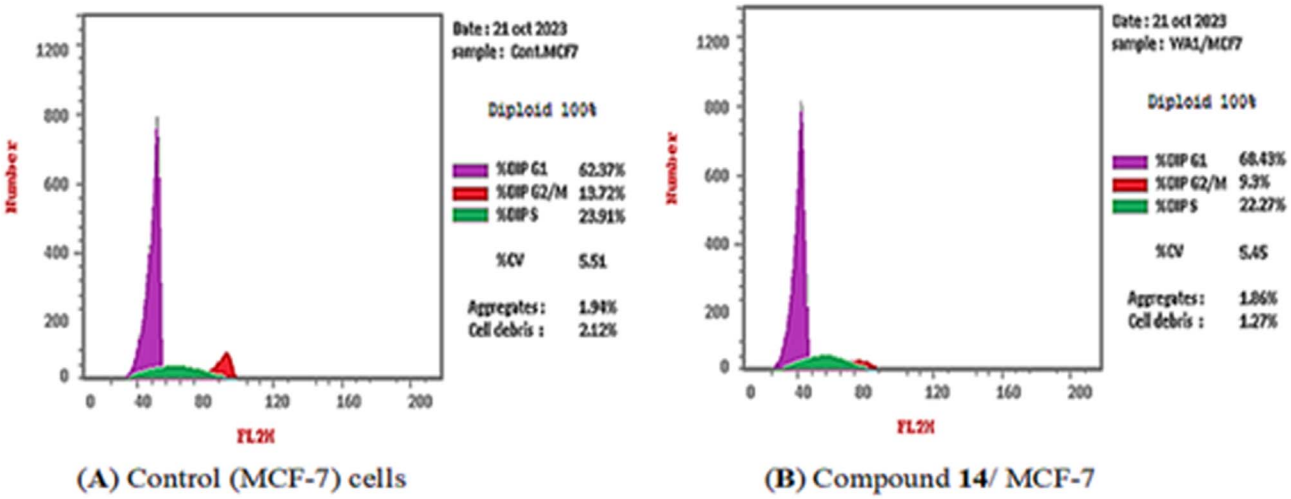


Fig. 4 Cell cycle distribution of MCF-7 cells as determined by flow cytometry. (A) Control and (B) compound **14**.

Table 4 The impact of compound **14** on the various stages of cell death in MCF-7 cells

| Sample | Total apoptosis (%) | Early apoptosis (%) | Late apoptosis (%) | Necrosis (%) |
|---|---|---|---|---|
| Compound **14**-treated MCF-7 cells | 52.05 | 16.53 | 29.57 | 5.95 |
| MCF-7 cells | 2.28 | 0.61 | 0.24 | 1.43 |

the ability of compound **14** to inhibit the healing and migration of the treated cells.

### 3.3. Computational studies

**3.3.1. DFT studies.** The DFT methodology was applied using the B3LYP/6-31+G(d,p) method without symmetry restrictions using Gaussian09 (D.01) software to examine the electronic and structural characteristics of compound **14**. Using the chosen approach, the theoretical optimization of the WM-3 molecular structure was completed and is shown in Fig. 7a. Subsequently, quantum chemical characteristics like total energy and dipole moment (Dm) are listed in Table 7.

The title molecule's non-planarity may be seen in the optimized geometric structure, which has 222 electrons and 51 atoms. The two terminal benzene rings are slightly angled towards the average plane of the molecule, according to geometry optimization, and the optimized geometrical parameter TE, or total ground energy, is −46546.1 eV. The same level of theory was used to estimate the electronic dipole moment (Dm), which is large (8.516 Debye), indicating considerable charge separation. The HOMO–LUMO gap ($E_{gap}$), a crucial indicator of kinetic stability, was calculated after the quantum evaluation of HOMO and LUMO energies, as shown in Fig. 7b. Chemical reactivity and the HOMO/LUMO border orbitals have a strong relationship as low reactivity is indicated by high molecular orbital gap values ($E_{gap}$). The small $E_{gap}$ indicates that the produced drug has high chemical reactivity because of charge transfer interactions. Subsequently, the Gauss Sum 3.0 program calculated the gas phase's density of states (TDOS). The TDOS diagram for compound **14** is shown in Fig. 7c.

Table 5 Effect of compound **14** on levels of BAX and Bcl-2 in MCF-7 cells

| | RT-PCR fold change | |
|---|---|---|
| Sample | Bcl2 | BAX |
| Compound **14** | 0.159 | 6 |
| Control MCF-7 cells | 1 | 1 |

Koopman's' hypothesis was used to study the global reactivity descriptors; the values in Table 7 of the ESI† are used. Due to its high HOMO energy and low HOMO–LUMO $E_{gap}$, which indicate significant inhibitory reactivity, the molecule under examination exhibits a high softness ($\sigma$) and a low hardness ($\mu$). A further property indicated in Table 7 that is used to assess the inhibitory reactivity and quantify a compound's capacity to absorb electrons from the target is the electrophilicity index ($\omega$). The results showed that the title compound has significant inhibitory reactivity.[62]

Mulliken atomic charge distribution is a common technique for calculating inhibitory sites for adsorption. The investigated compound has good ability to bond with the target surface using the donor–acceptor method, as shown in Fig. 7d. The highest positive charge was found at **C15** while **C20** acquired the highest negative atomic charge.

For predicting drug–receptor connections, surface molecular electrostatic potential (ESP) can be mapped using DFT. The ESP

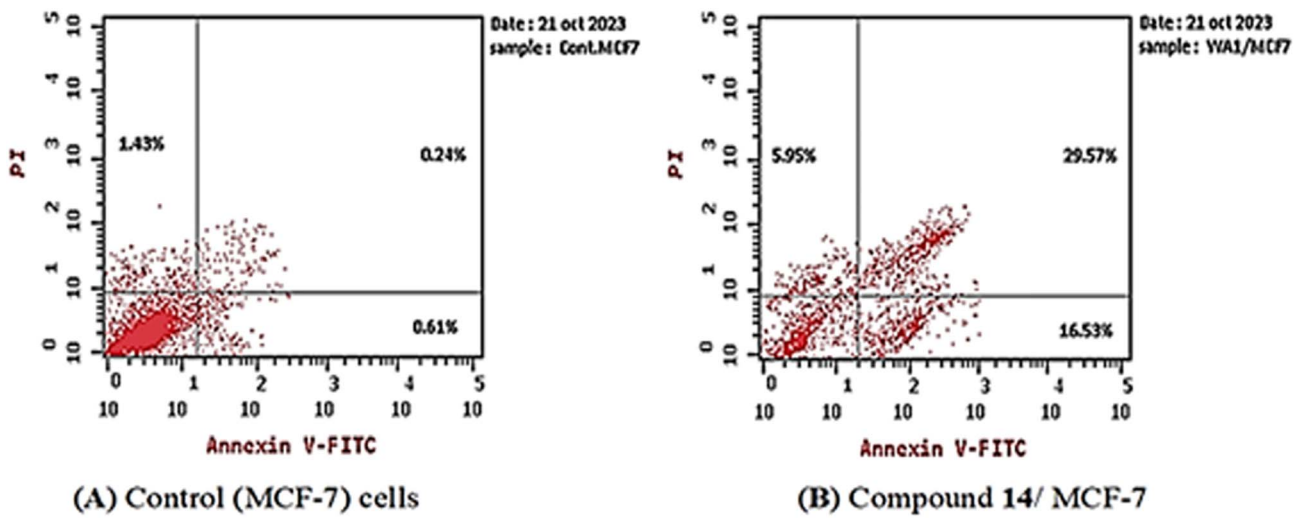


Fig. 5 Compound **14** induced apoptosis in MCF-7 cells. (A) Control and (B) compound **14**.

 

Table 6 The effect of compound **14** on the migration and healing of MCF-7 after 48 h

| Item | At 0 h | | At 24 h | | At 48 h | | | | |
|---|---|---|---|---|---|---|---|---|---|
| | Area ($\mu m^2$) | Width ($\mu m$) | Area ($\mu m^2$) | Width ($\mu m$) | Area ($\mu m^2$) | Width ($\mu m$) | RM ($\mu m$) | Wound closure (%) | Area difference (%) |
| Control MCF-7 cells | 876.333 | 875.422 | 673.000 | 672.059 | 284.333 | 283.351 | 12.335 | 67.554 | 592.000 |
| MCF-7 cells treated with 14 | 933.000 | 932.006 | 836.333 | 835.443 | 571.333 | 570.472 | 7.532 | 38.764 | 361.667 |

increases recognition of electrophilic interactions, substituent impacts, inhibitory reactivity, and both inter- and intra-bonding forces after being connected to the active sites of the prepared compound. Red (electron-rich), yellow (slightly electron-rich), blue (electron deficient), and green (neutral zone) are the colors in which the value of ESP increases. Fig. 7e shows that the blue zone of the drug is localized over the hydrogen atoms, whereas the red and yellow portions are generated by the lone pair of oxygen atoms. The ring system is encircled by neutral green. As a result, the drug's electrophilic active sites are anticipated to be located around the hydrogen atoms, while the negative electrostatic potential is encapsulated over the oxygen and nitrogen atoms, making this the preferred location for electrophilic assault by the target sites.[63]

Microelectronic and structural investigations might not be sufficient to completely comprehend a drug's intermolecular interactions. Consequently, charge density parameters were evaluated using the Multiwfn and AIMALL programs. These programs enable the computation of topological features such as electronic charge density ($\rho$), total electron energy density ($H(r)$), Laplacian of electronic charge density ($\nabla^2\rho$), and the two components of $H(r)$; kinetic electron energy density ($G(r)$ and potential electron energy density ($V(r)$) at the bond critical points (BCP). These computations are possible *via* the Quantum Theory of Atoms in Molecules (QTAIM).

Table S1† makes it clear that the values of $\nabla^2\rho$ and $H(r)$ are negative, suggesting that all BCP connections are covalent except for **N14–H33** and **N14–H36**, which have weak electrostatic attractions. The relief map in Fig. 7f depicts the electron density ($\rho$) in the XY plane, whereas Fig. 7g shows all bond paths within the compound.

**3.3.2. Molecular docking study.** The newly designed 5-acetyl-1,3,4-thiadiazol-2(3*H*)-ylidene derivatives were exposed to molecular docking processes to evaluate their inhibitory activity towards the VEGFR-2 receptor. After completion of the docking processes, the best pose for the frontier candidate **14** was selected for further investigation. Observing the binding pose of sorafenib, a standard VEGFR-2 inhibitor, inside the VEGFR-2 active pocket, it was evident that it became stabilized by creating crucial hydrogen bonds with Glu883 and Asp1044 *via*

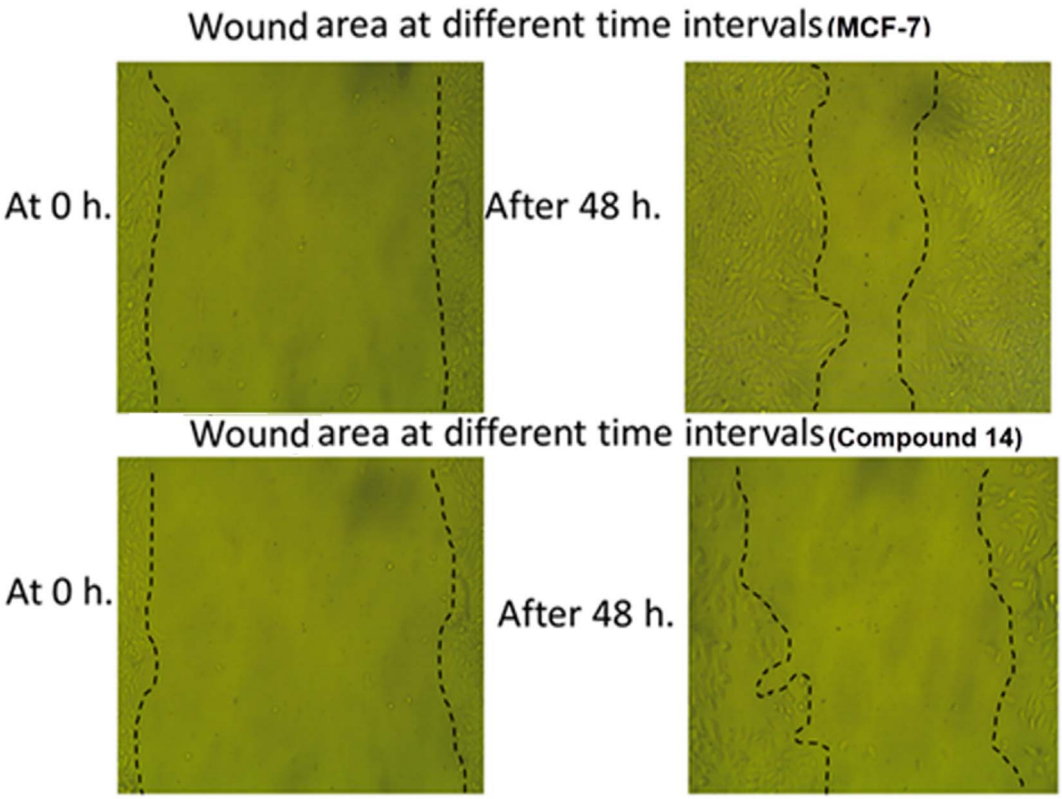


Fig. 6 The impact of compound **14** on migration and healing of MCF-7 cells after 48 h.

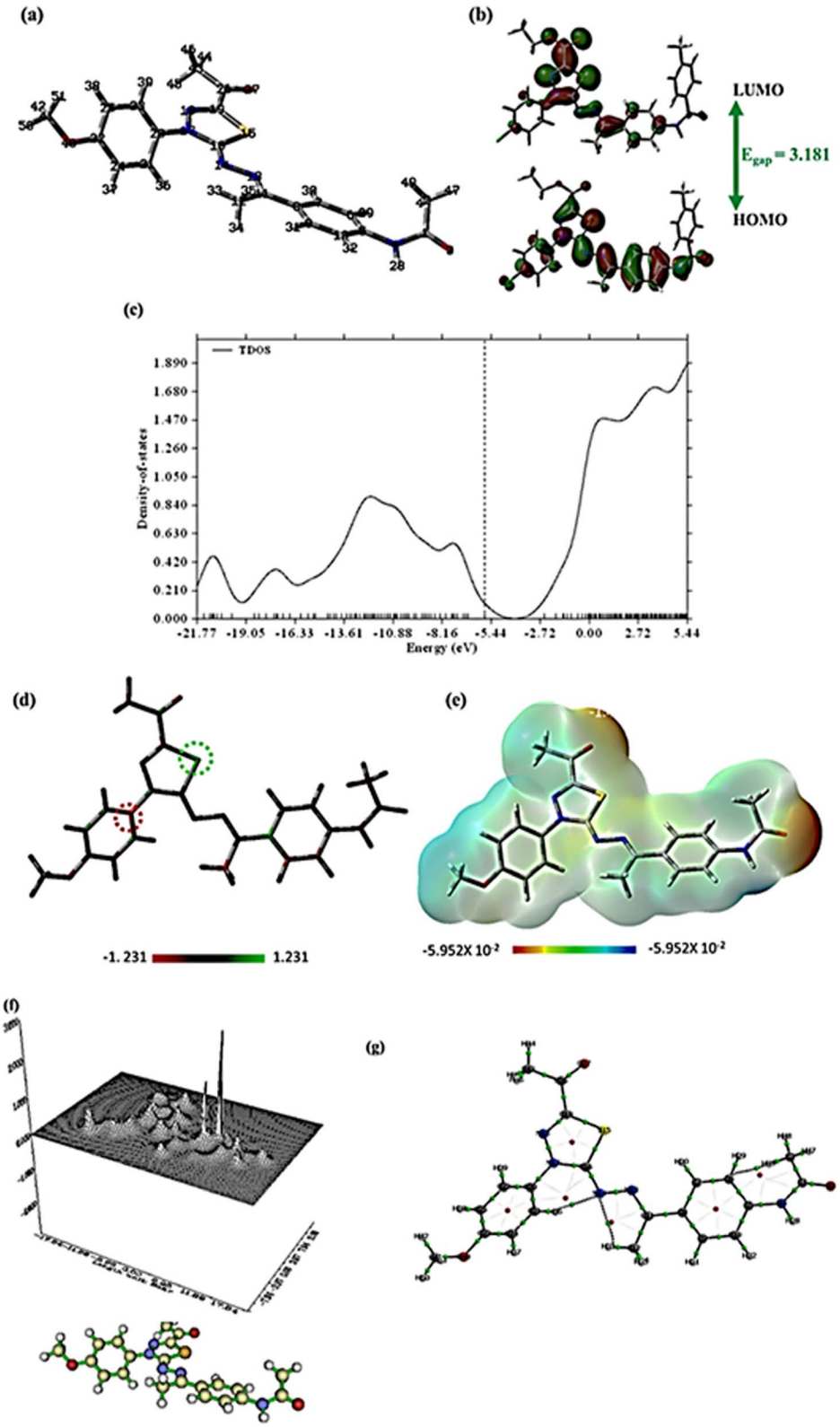


Fig. 7 The full optimized geometry (a), FMO and energy gap (b), TDOS spectrum (c), Mullikan atomic charge distribution (d), ESP (e), and the QTAIM maps (f) and (g) at B3LYP/6-31+G(d,p) for the chosen molecule **14**.

its urea group (hydrogen bond donor–acceptor moiety). Additionally, through the *N*-methylpicolinamide moiety, it added another hydrogen bond to Cys917. Moreover, the terminal 4-chloro-3-(trifluoromethyl)phenyl) moiety was buried inside the hydrophobic pocket *via* pi–pi interactions with Leu887, Ile886, and Ile890 (Table 8).

Table 7 The DFT-calculated global reactivity parameters for compound **14**

| IP | EA | $\mu$ (eV) | $\chi$ (eV) | $\eta$ (eV) | $\sigma$ (eV) | $\omega$ (eV) | Dm (Debye) | TE (eV) | $\Delta N_{max}$ | $\Delta E$ (eV) |
|---|---|---|---|---|---|---|---|---|---|---|
| 5.653 | 2.472 | −4.063 | 4.063 | 1.591 | 0.629 | 13.126 | 8.516 | −46546.1 | 2.554 | −13.126 |

Herein, the examined molecule (**14**) kept the crucial hydrogen bonds to Glu883 and Asp1044 through its amide group verifying its positioning with the identical orientation inside the VEGFR-2 active pocket (Table 8). In addition, it formed two electrostatic interactions with Cys917 and Phe1045 in the hinge region through its 5-acetyl-3-(4-methoxyphenyl)-1,3,4-thiadiazole moiety. Furthermore, additional electrostatic and pi–pi interactions were observed in the linker area between the central phenyl moiety and Cys1043 and Val846, respectively. Thus, the results discussed above strongly support candidate **14**'s extremely promising inhibitory capability towards the VEGFR-2 target receptor. This may be why it produced better biological outcomes as a prospective VEGFR-2 antagonist when compared to the reference drug sorafenib.

**3.3.3. MD simulation studies.** During the simulation, the stability of the reference system (VEGFR-2–sorafenib) and VEGFR-2–compound **14** was assessed using root-mean-square deviation (RMSD) values. The RMSD values for the reference system remained consistently stable at approximately 2.5 Å, as indicated by the red line. In contrast, VEGFR-2 in VEGFR-2–compound **14** initially exhibited an increasing trend for the first 75 ns of the simulation, followed by a decrease in the next 35 ns. It eventually reached a stable state for the last 90 ns, with an average value of 3.7 Å (Fig. 8A). The RMSD of compound **14** showed two distinct states during the simulation. For the first 65 ns, the RMSD of compound **14** hovered around 3.5 Å. However, in the remaining duration of the simulation, the RMSD nearly doubled to approximately 7 Å (Fig. 8B). This sudden rise was attributed to a conformational change of the ligand while still maintaining its binding to the protein, as depicted in Fig. 8C which shows the ligand in two different conformations. The first conformation, shown in red sticks,

Table 8 2D interactions and mapping surfaces of thiadiazole derivatives and sorafenib within the active site of VEGFR-2 (PDB ID: 2OH4)

| Compound | 2D interaction | Mapping surface |
|---|---|---|
| Sorafenib | 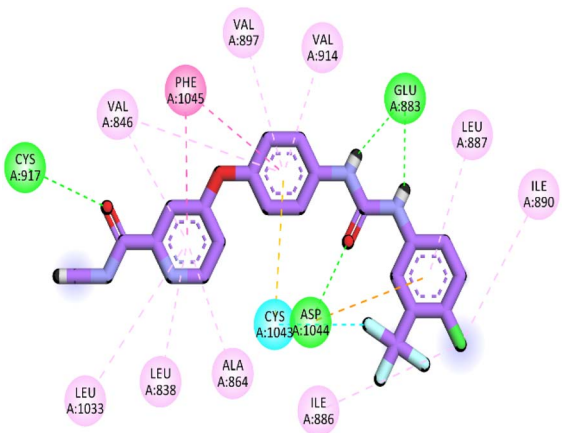 | 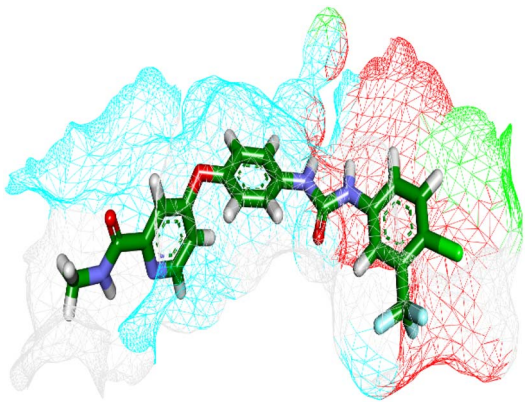 |
| **14** | 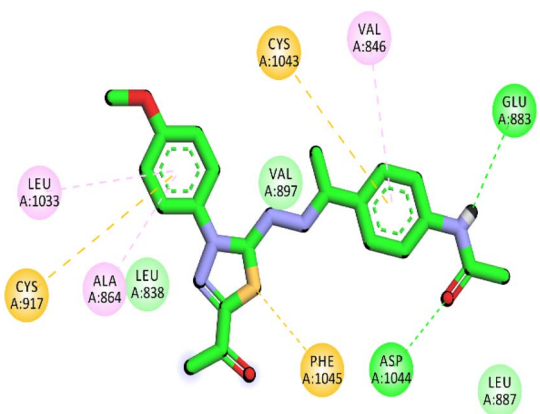 | 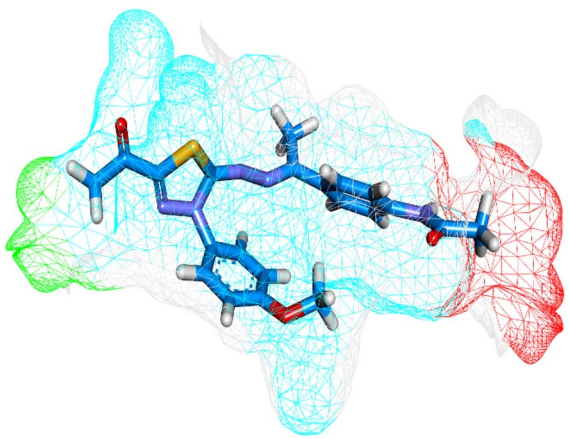 |

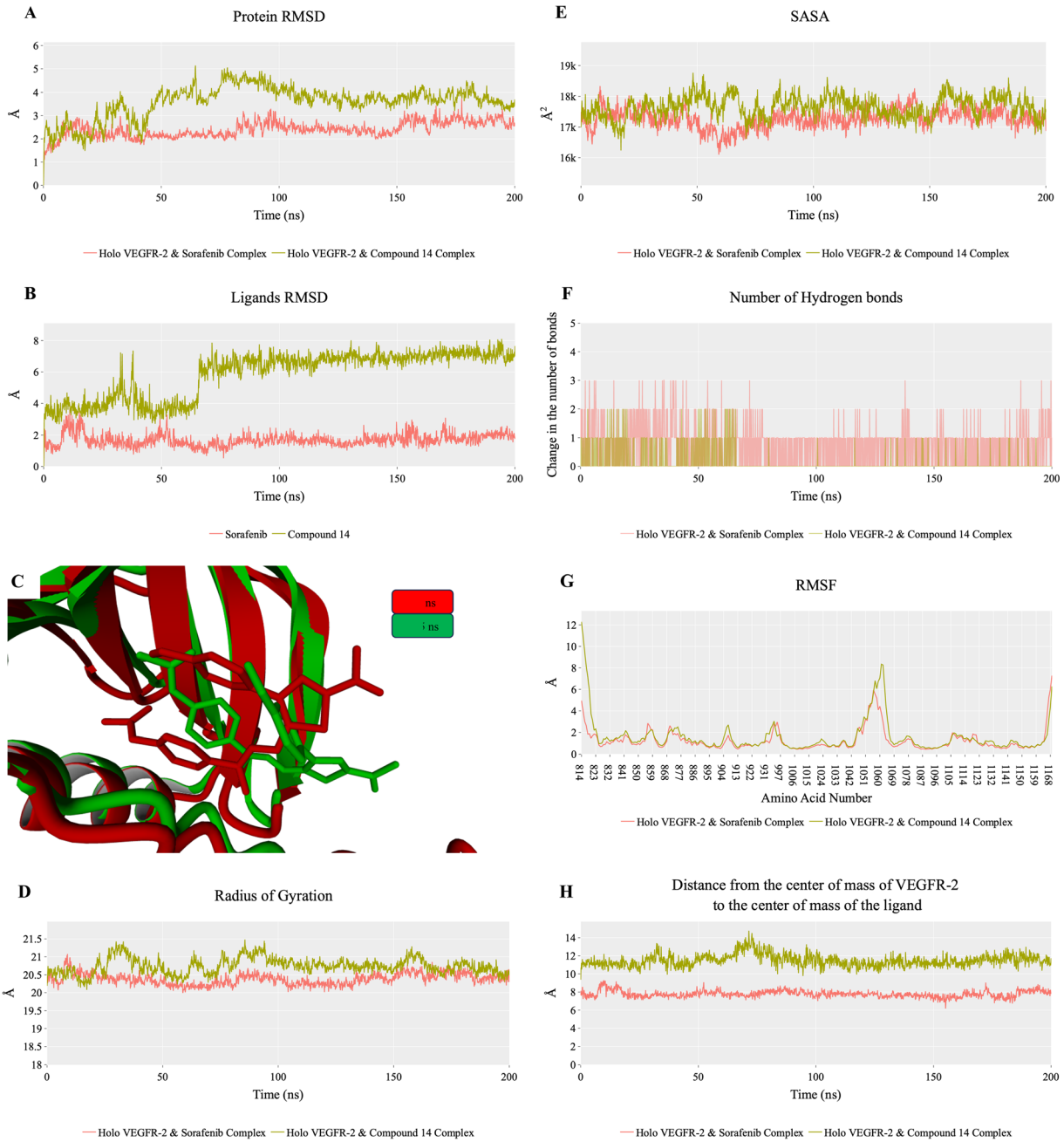


Fig. 8 MD results for VEGFR-2–sorafenib complex (red line) and VEGFR-2–compound **14** complex (dark green line): (A) RMSD values from the trajectory for VEGFR-2. (B) Compound **14** RMSD values. C) Comparison between compound **14** conformation at 0 ns (green sticks) and 20 ns (cyan sticks) showing the fluctuation of a part of compound **14**. (D) RoG. (E) SASA. (F) Alteration in the count of hydrogen bonds between sorafenib (red) or compound **14** (dark green) and VEGFR-2. (G) RMSF. (H) The distance between the center of mass of sorafenib (red) or compound **14** (dark green) and the VEGFR-2 protein.

occurred at 20 ns, while the second conformation, shown in green sticks, occurred at 175 ns. In contrast, sorafenib displayed a more consistent pattern with an average RMSD of approximately 1.5 Å, shown as a red line. Fig. 8D and E indicate slight variations in the average radius of gyration (RoG) and solvent-accessible surface area (SASA) between the two systems, respectively. Fig. 8F demonstrates that compound **14** maintained one hydrogen bond for the initial 65 ns, before changing its conformation, and then showed almost no detectable H-bonds for the remaining time. On the other hand, sorafenib exhibited fluctuations between one and two hydrogen bonds, indicating a stronger interaction with the protein. The RMSF values showed a similar pattern in the two systems, with the N-terminal region of VEGFR-2–compound **14** having more fluctuations compared to the reference system (Fig. 8G). Compound **14** consistently had an average distance of around 11 Å between the protein's center of mass and the ligand, indicating a stable

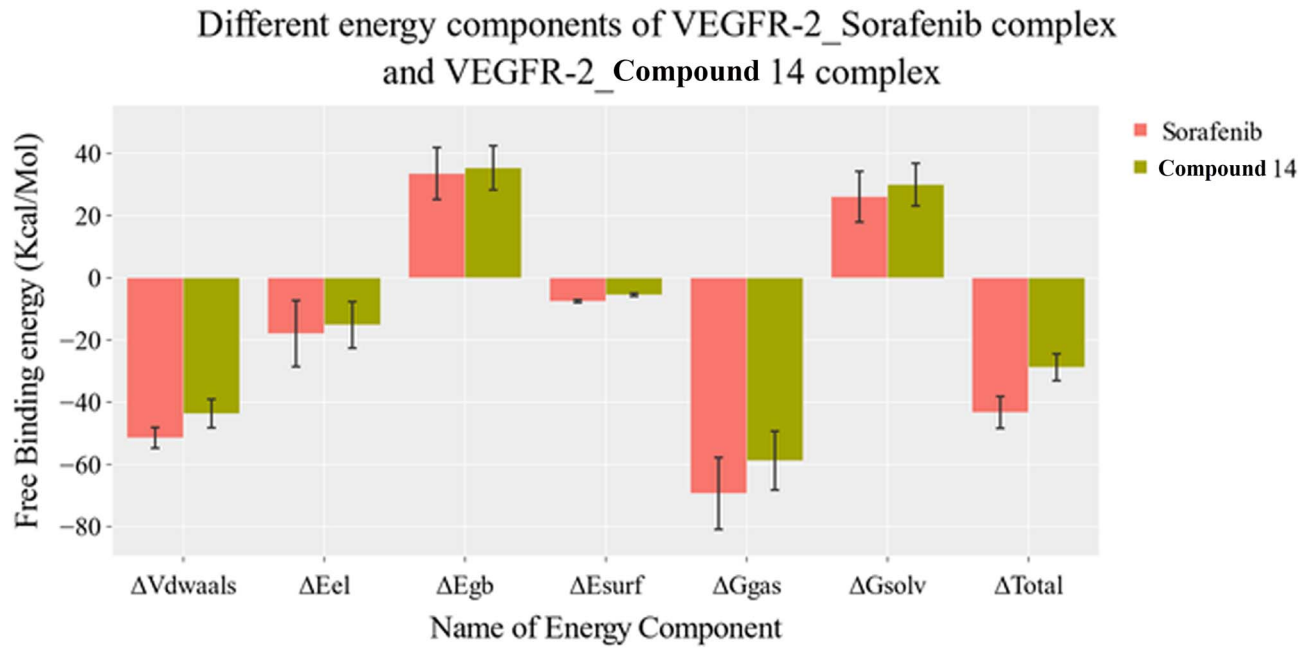


Fig. 9 MM-GBSA analysis as well as the detailed values for both systems. Bars represent the standard deviations.

interaction (Fig. 8H), although this distance was about 3 Å higher than for the reference compound.

**3.3.4. Molecular mechanics-generalized born surface area (MM-GBSA).** The components involved in calculating the binding free energy using the MM-GBSA method are shown in Fig. 9. There is a moderate difference in the binding energy between compound **14** (−28.77 kcal $mol^{-1}$) and sorafenib (−43.25 kcal $mol^{-1}$), indicating some variations in the factors that influence binding. van der Waals interactions are slightly more important for maintaining the stability of sorafenib compared to compound **14** (−51.4 kcal $mol^{-1}$ *vs.* −43.61 kcal $mol^{-1}$). Similarly, sorafenib has slightly better

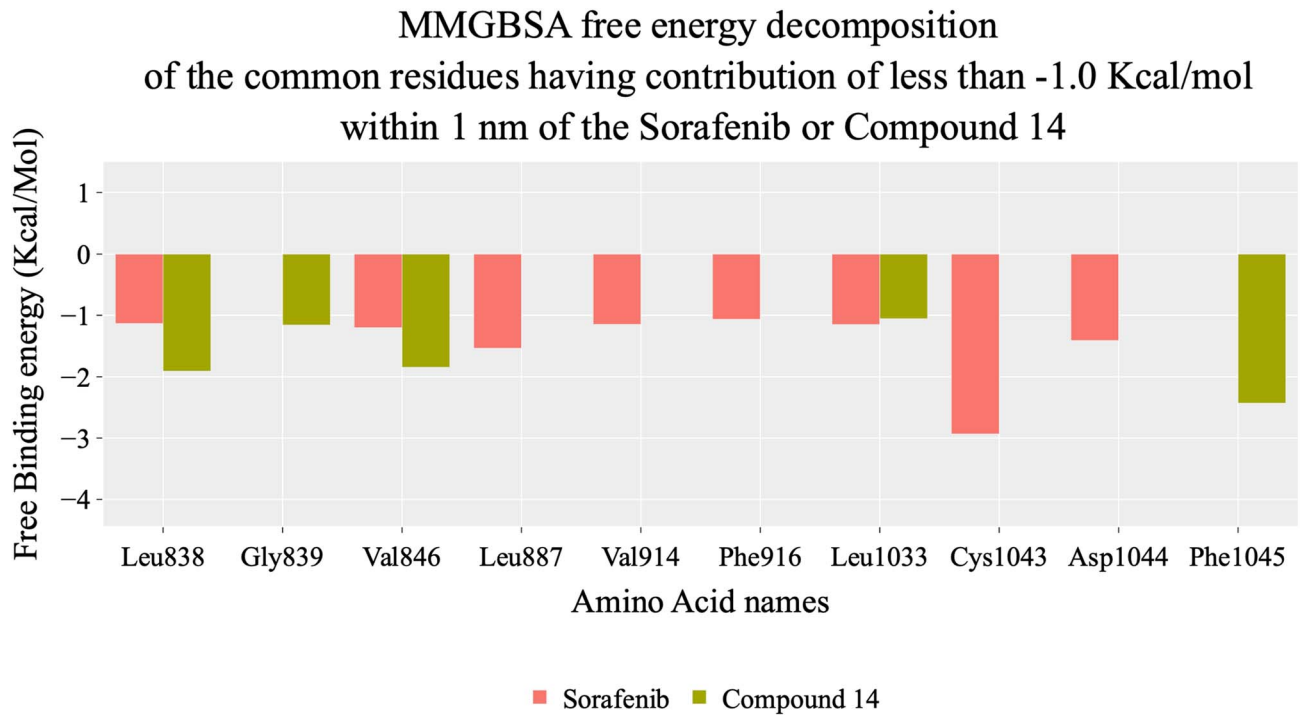


Fig. 10 A comparison of the free binding energy decomposition of the VEGFR-2–compound **14** and VEGFR-2–sorafenib complexes. Amino acids shown are the ones within 1 nm of each ligand, common between the two systems and having a binding affinity of −1 kcal $mol^{-1}$ or better.

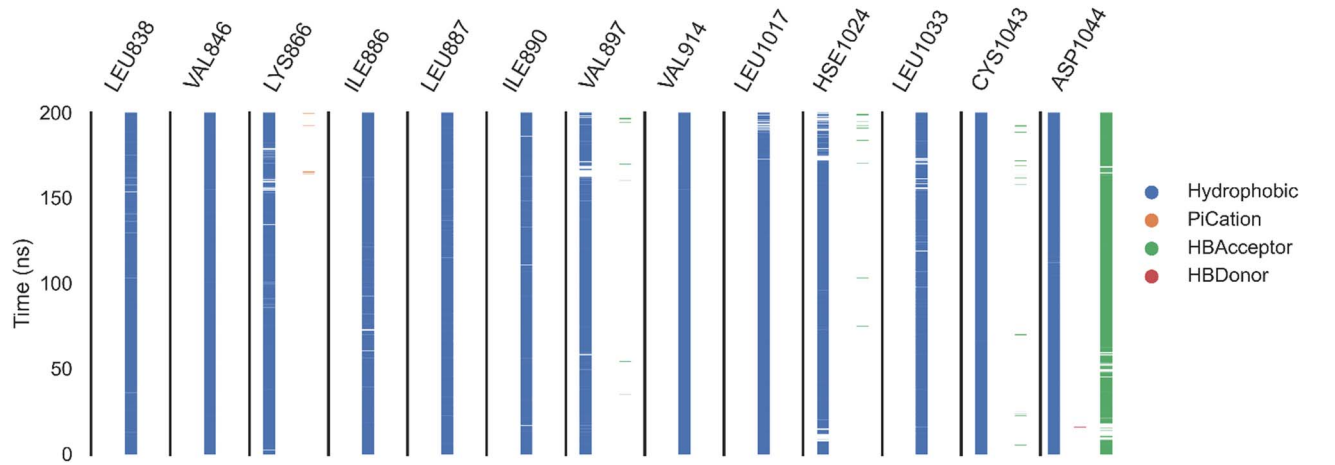


Fig. 11 The amino acids, the types of interactions with sorafenib, and their occurrence during the whole simulation time using the ProLIF python library.

electrostatic interactions than compound **14** (−17.92 kcal mol$^{-1}$ *vs.* −15.13 kcal mol$^{-1}$). The contribution of individual amino acids within 1 nanometer proximity to each ligand was assessed using decomposition analysis (Fig. 10). Four amino acids, Leu838, Gly839, Val846, and Phe1045, were found to have a more significant impact on the binding of compound **14**, compared to sorafenib. Specifically, Leu838 had energy contributions of −1.9 kcal mol$^{-1}$ (compound **14**) and −1.13 kcal mol$^{-1}$ (sorafenib), Gly839 had contributions of −1.15 kcal mol$^{-1}$ (compound **14**) and +0.02 kcal mol$^{-1}$ (sorafenib), Val846 had contributions of −1.84 kcal mol$^{-1}$ (compound **14**) and −1.2 kcal mol$^{-1}$ (sorafenib), and Phe1045 had contributions of −2.43 kcal mol$^{-1}$ (compound **14**) and −0.86 kcal mol$^{-1}$ (sorafenib). On the other hand, sorafenib had six amino acids with a greater contribution to its stability compared to compound **14**.

**3.3.5. Protein–ligand interaction fingerprint (ProLIF).** We used the ProLIF method to determine which amino acids are

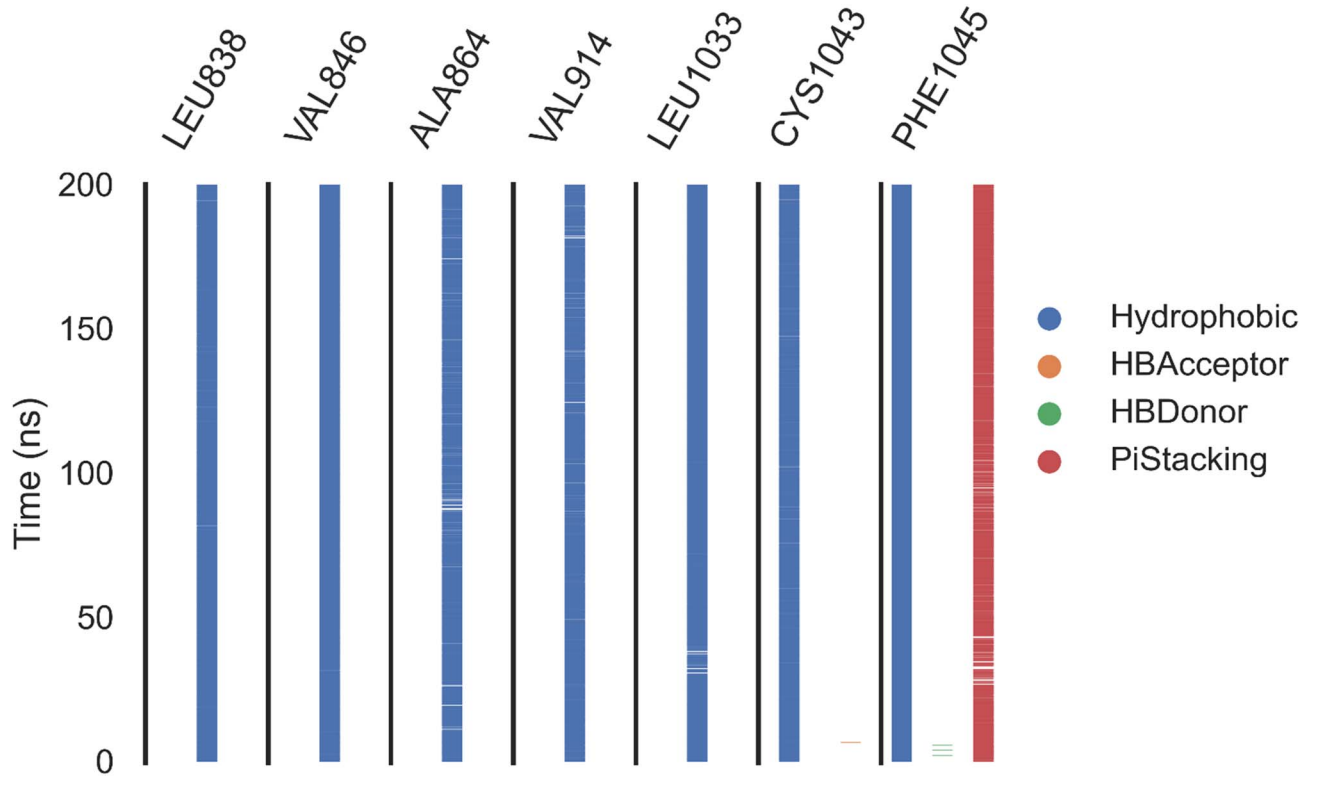


Fig. 12 The amino acids, the types of interactions with compound **14**, and their occurrence during the whole simulation time using the ProLIF python library.

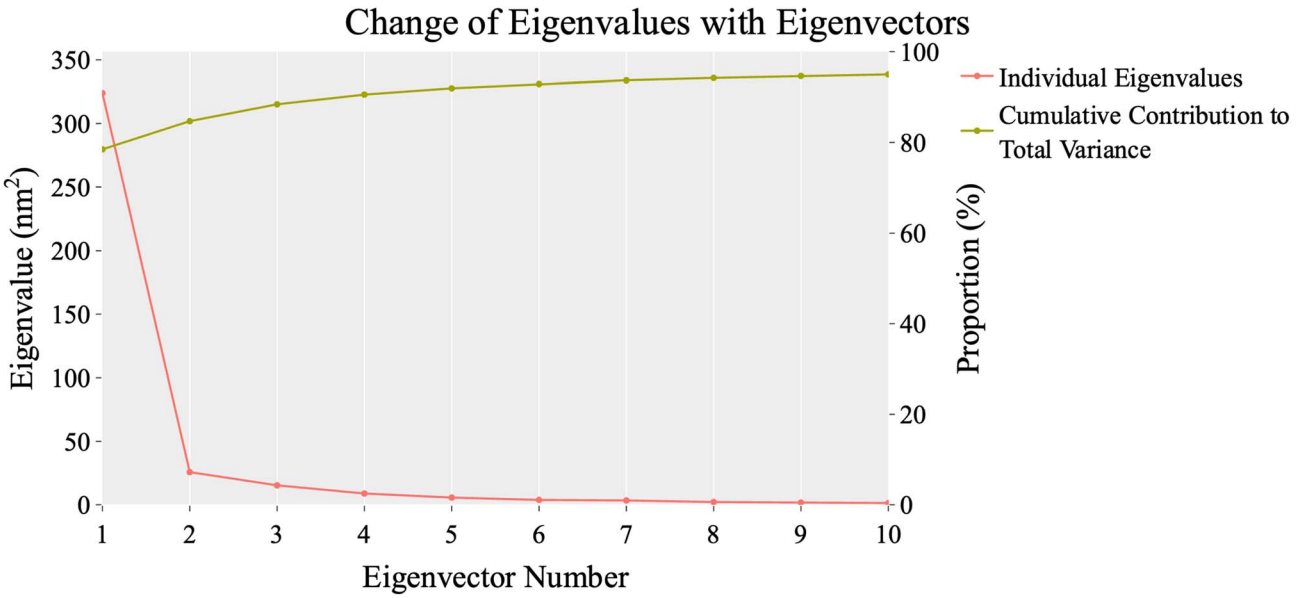


Fig. 13 The change in eigenvalues with increasing eigenvectors (blue line). In addition, the cumulative variance retained in the eigenvectors is shown (red line).

involved in ligand interactions. Our analysis of sorafenib's trajectory identified 13 amino acids that have a hydrophobic binding occurrence of over 80%. These amino acids are Leu838 (91.2%), Val846 (98.6%), Lys866 (87.9%), Ile886 (92.9%), Leu887 (95.1%), Ile890 (95.2%), Val897 (88.9%), Val914 (99.7%), Leu1017 (95.4%), His1024 (86.6%), Leu1033 (91%), Cys1043 (99.8%), and Asp1044 (99.3%). These amino acids are the main ones involved in interactions with sorafenib, as shown in Fig. 11. Additionally, Asp1044 has a hydrogen bond formation rate of 88.2%. In contrast, compound **14** formed hydrophobic interactions with seven amino acids, achieving a minimum rate of 80% (Fig. 12). These amino acids are Leu838 (97.8%), Val846 (99.2%), Ala864 (86%), Val914 (88.8%), Leu1033 (96.8%), Cys1043 (93.4%), and Phe1045 (100%). Furthermore, Phe1045 exhibited a notable pi-stacking rate of 82.6%. Among these seven amino acids, five were shared with the reference compound, suggesting a moderate and similar mode of interaction. Additionally, three of these amino acids displayed stronger and more significant contributions compared to the reference compound, as depicted in Fig. 11.

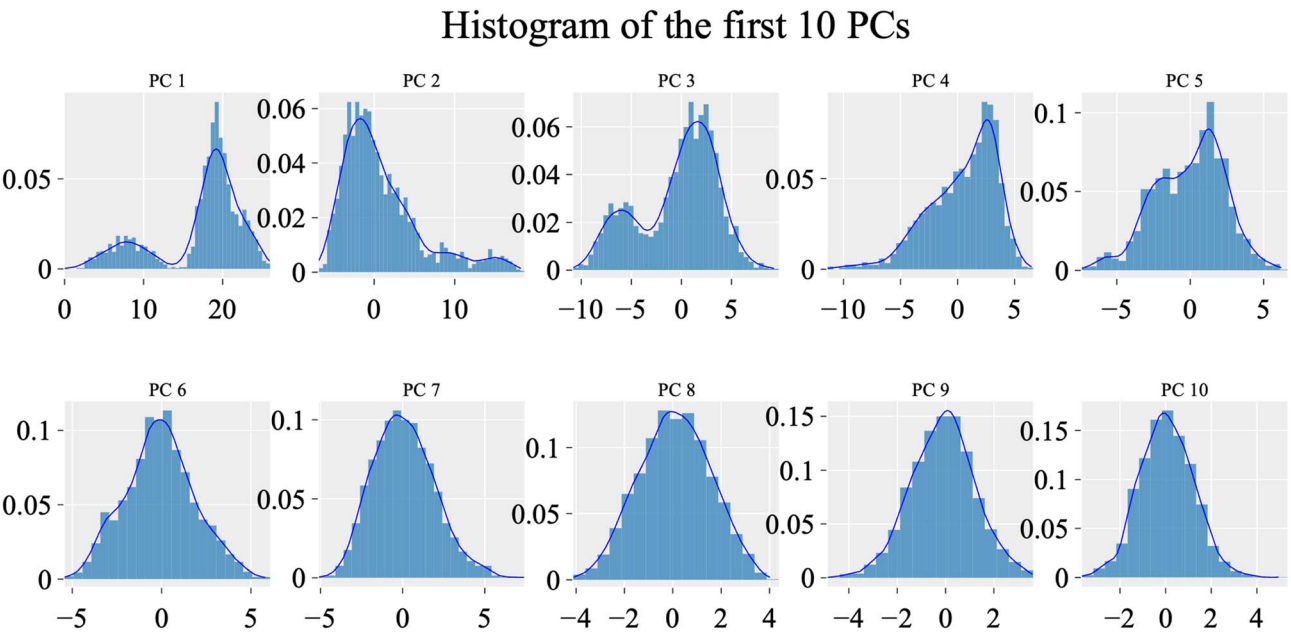


Fig. 14 The distribution of the first ten eigenvectors.

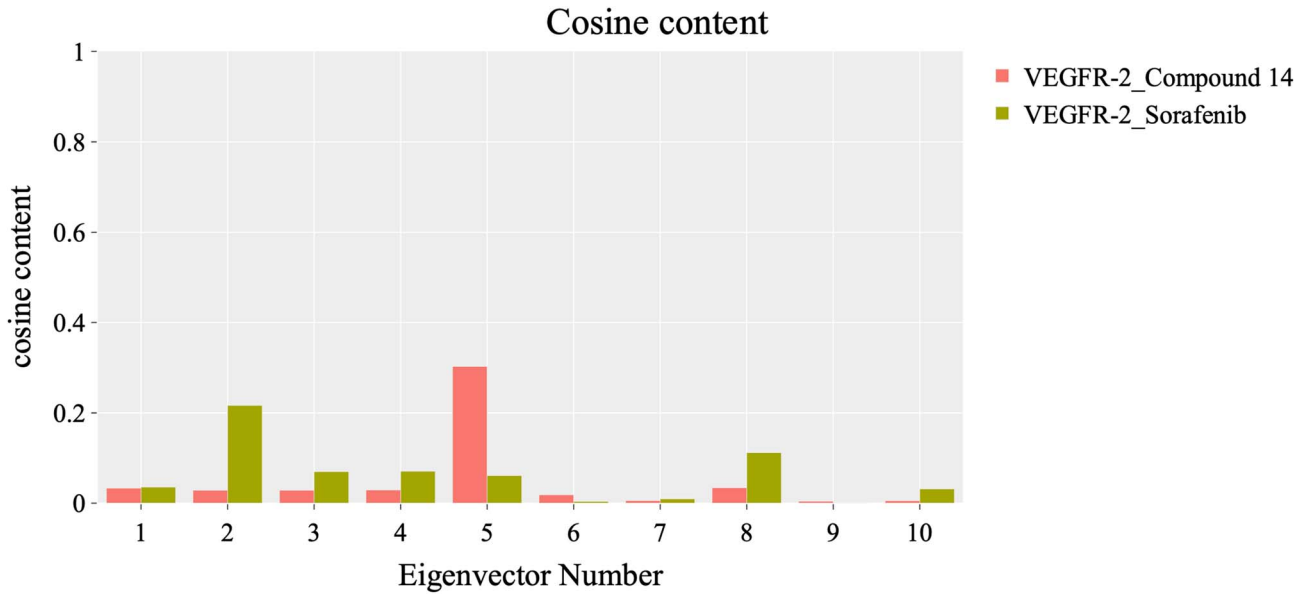


Fig. 15 Values of the cosine content of the first ten eigenvectors for the two trajectories.

**3.3.6. Principal component analysis of trajectories (PCAT).** To identify synchronized movements, we used PCAT. We considered various factors as outlined in the methods section to determine the appropriate size of the reduced subspace. These factors included the scree plot, eigenvector distribution, and cumulative variance preserved by additional eigenvectors. The scree plot showed a clear decrease in slope starting from the second principal component (PC). The first eigenvector alone accounted for approximately 78% of the total variance, while the combined contribution of the first three eigenvectors explained around 88% of the overall variance (Fig. 13). It is important to note that the distribution of the first five PCs did not follow a Gaussian pattern (Fig. 14). Therefore, we decided to use the top three eigenvectors as representatives of the fundamental subspace.

To evaluate the degree of randomness in the behavior of the first ten eigenvectors, we calculated the cosine content for both systems (Fig. 15). Our analysis revealed that, with the exception of the second principal component of the VEGFR-2–sorafenib system (0.21) and the fifth PC value of the VEGFR-2–compound **14** system, the cosine content of the first 10 eigenvectors remained below 0.2 in both systems. Furthermore, the root-mean-square inner product (RMSIP) indicated a limited overlap between the two subspaces, especially for the first three eigenvectors, which had an overlap of approximately 16%. Additionally, the RMSIP analysis showed that the C matrices of

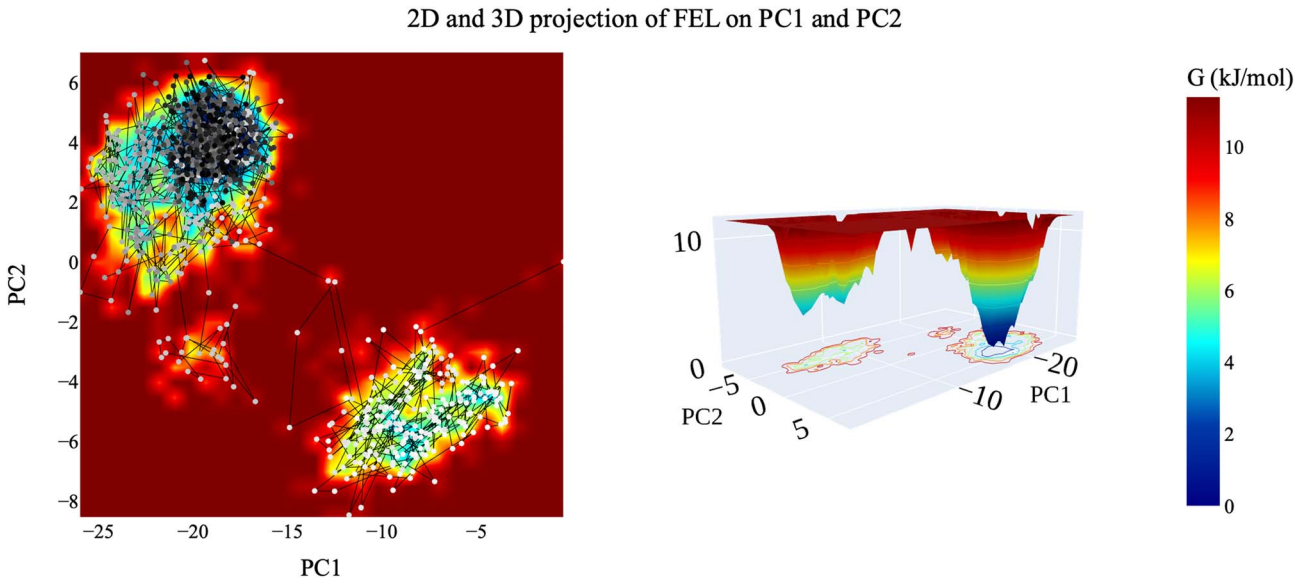


Fig. 16 The 2D and 3D projection of the VEGFR-2–compound **14** trajectory's FEL on the first two eigenvectors.

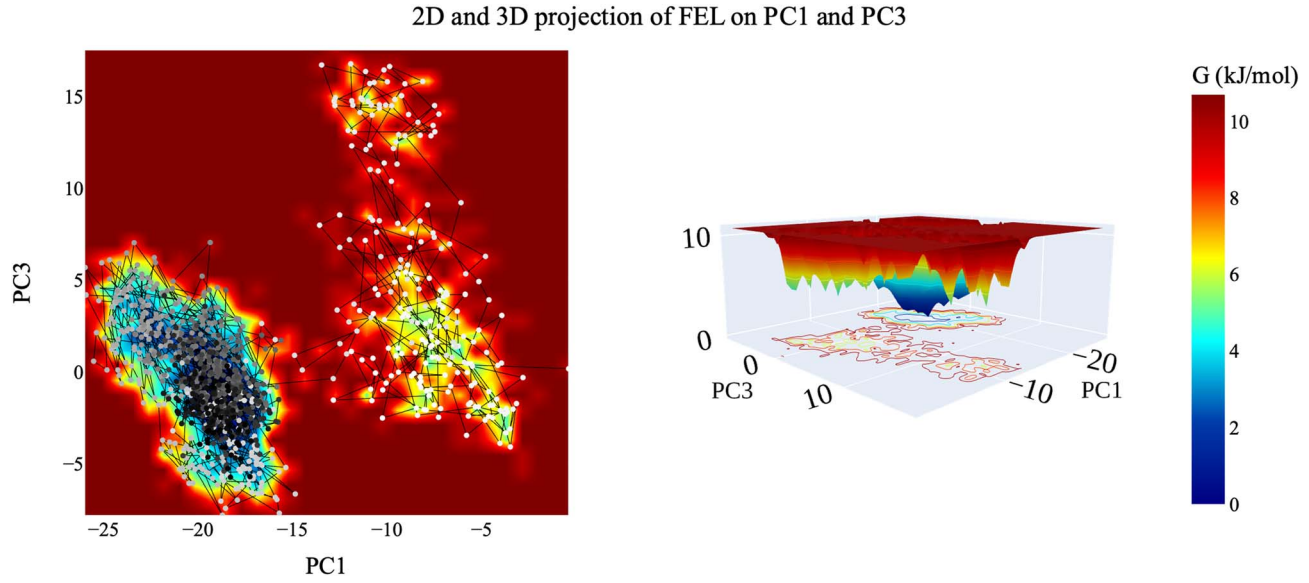


Fig. 17 2D and 3D projection of the VEGFR-2–compound **14** trajectory's FEL on the first and third eigenvectors.

the two systems were only 27.9% similar, indicating distinct sampling characteristics for each system.

**3.3.7. Free energy landscape (FEL).** We analyzed the trajectory of VEGFR-2–compound **14** by projecting it onto the FEL using different combinations of the first three principal components (PCs). We performed this projection using two PCs at a time, resulting in various basins, as shown in Fig. 16–18. All three figures exhibit a similar trend, starting with limited sampling in the initial frames (represented by white dots) and eventually converging to a global minimum (represented by black dots) towards the end of the simulation. The trajectory remains within this basin for a significant duration, with no significant fluctuations observed between the two regions, as indicated by the connecting line between the frames. In particular, the projection onto the first two PCs (Fig. 16) reveals an initial sampling that differs from the basin observed at the end of the simulation, with a difference of 3.81 kJ $mol^{-1}$. Additionally, the basin is narrow, suggesting a limited number of conformations. In contrast, Fig. 17 illustrates the PC1–PC3 projection, which reveals a broad basin containing a single wide global minimum. The difference in energy between the initial sampling minima and the global minimum was calculated to be 4.46 kJ $mol^{-1}$. Likewise, Fig. 18 displays the projection on the PC2 and PC3, demonstrating a wide global minimum with a 3.39 kJ $mol^{-1}$ difference between the two regions.

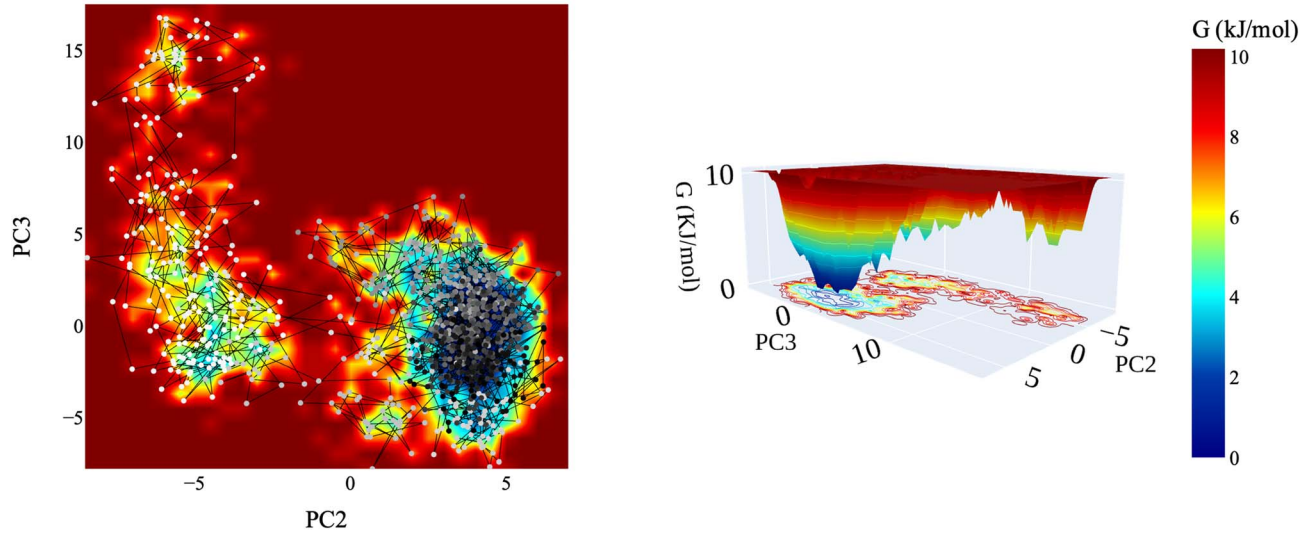


Fig. 18 The 2D and 3D projection of the VEGFR-2–compound **14** trajectory's FEL on the second and third eigenvectors.

Table 9 ADMET screening of the derivatives **14** and **18a–f**

| Compound | BBB level | Solubility level | Absorption level | CYP2D6 prediction | PPB prediction |
|---|---|---|---|---|---|
| **14** | Low | Low | Good | Non-inhibitors | Less than 90% |
| **18a** | Very low | Very low | Moderate | | More than 90% |
| **18b** | | | | | |
| **18c** | | | | | |
| **18d** | | Low | Poor | | |
| **18e** | | | Moderate | | |
| **18f** | | Very low | Poor | | |
| Sorafenib | | | Good | | |

Table 10 Toxicity study of the derivatives **14** and **18a–f**

| Compound | Carcinogenic potency $TD_{50}$ (mouse) [a] | Ames prediction | FDA rodent carcinogenicity (mouse–female) | Rat oral $LD_{50}$ [b] | Rat chronic LOAEL [b] | Skin irritancy | Ocular irritancy |
|---|---|---|---|---|---|---|---|
| **14** | 25.1941 | Non-mutagen | Non-carcinogen | 0.307791 | 0.0340816 | Non-irritant | Mild |
| **18a** | 19.1051 | | | 0.211142 | 0.0407246 | | |
| **18b** | 10.1397 | | | 0.342938 | 0.0653748 | | |
| **18c** | 5.86494 | | | 0.147569 | 0.012965 | | |
| **18d** | 3.51292 | | | 0.292276 | 0.0298888 | | |
| **18e** | 10.9809 | | | 0.357591 | 0.0180164 | | |
| **18f** | 5.82645 | | | 0.580656 | 0.0289143 | | |
| Sorafenib | 19.2359 | | Single-carcinogen | 0.822583 | 0.00482816 | | |

[a] Unit: mg $kg^{-1}$ $day^{-1}$. [b] Unit: g $kg^{-1}$.

**3.3.8. *In silico* ADMET analysis.** The *in silico* ADMET results offered an initial predicted overview of the pharmacokinetic profiles of the synthesized seven thiadiazole derivatives relative to the benchmark drug, sorafenib (Table 9). It is noteworthy that all compounds demonstrate a pronounced deficiency in blood–brain barrier permeability, signifying limited access to the central nervous system. This characteristic suggests a focus on peripheral rather than central cancer targets. Furthermore, their generally low aqueous solubility raises considerations about potential challenges in achieving optimal drug concentrations in biological fluids. Despite these solubility concerns, the compounds display good human intestinal absorption levels accompanied by a consistent tendency towards high plasma protein binding (except compound **14**), which could impact their distribution and clearance kinetics. Additionally, the absence of CYP2D6 inhibition across the compounds implies a lower likelihood of interactions with drugs metabolized by this essential enzyme. These results collectively provide crucial initial insights, setting the stage for further experimental validation and refinement in the pursuit of effective therapeutic agents.

**3.3.9. *In silico* toxicity analysis.** The *in silico* toxicity results revealed promising safety profiles for the new thiadiazole derivatives in comparison to the established drug sorafenib (Table 10). In terms of carcinogenic potency, the derivatives exhibit lower values (ranging from 3.51 to 25.19 mg $kg^{-1}$ $day^{-1}$) compared to sorafenib (19.24 mg $kg^{-1}$ $day^{-1}$), indicating a potentially reduced risk of carcinogenic effects. All compounds, including sorafenib, are predicted to be non-mutagenic and non-carcinogenic according to the Ames test and the FDA rodent carcinogenicity (mouse–female) test, respectively. In acute toxicity assessments, the derivatives show oral $LD_{50}$ values ranging from 0.15 to 0.58 g $kg^{-1}$, with compound **18c** demonstrating the highest acute toxicity. Sorafenib exhibits a slightly higher oral $LD_{50}$ of 0.82 g $kg^{-1}$. In terms of chronic toxicity, the derivatives present chronic LOAEL values ranging from 0.01 to 0.07 g $kg^{-1}$, while sorafenib has a chronic LOAEL of 0.0048 g $kg^{-1}$, indicating much lower potential adverse effects with chronic exposure than that of sorafenib. Notably, all compounds, including sorafenib, are classified as non-irritants for skin and eyes, with mild irritancy noted for sorafenib. These findings suggest that the thiadiazole derivatives hold promise as potential alternatives to sorafenib, potentially offering reduced toxicity profiles, particularly in chronic exposure scenarios. Further experimental validation and dose-response studies are essential for a comprehensive assessment of their safety and efficacy for therapeutic applications.

## 4. Conclusion

In conclusion, in this study we successfully synthesized and comprehensively evaluated a series of thiadiazole derivatives designed to mimic VEGFR-2 inhibitors. Among the synthesized compounds, compound **14** emerged as a highly

 

promising candidate, displaying exceptional inhibitory properties against cancer cell lines MCF-7 and HepG2, as well as a remarkable affinity for VEGFR-2. Furthermore, compound **14** exhibited a unique ability to induce cell cycle arrest and apoptosis in MCF-7 cells, while also inhibiting cell migration and wound healing. Furthermore, compound **14** increased apoptosis by 6-fold while decreasing Bcl-2 levels (6.2-fold). The computational investigations confirmed the binding affinities, stability, and reactivity of compound **14**. Collectively, these findings strongly support compound **14** as a lead contender for further research in the development of anticancer drugs targeting VEGFR-2. This work lays a solid foundation for future advancements in the fields of anticancer- and angiogenesis-related research, driven by the potential of these thiadiazole derivatives.

## 5. Experimental

### 5.1. Chemistry

**5.1.1. General.** All apparatus, chemicals, and reagents are described in the ESI.†

**5.1.2. General procedure for the synthesis of intermediate 2.**

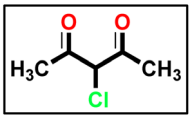

The synthesis of α-chloro-2,4-pentanedione **2** was carried out in accordance with the methodology described in ref. 55 with minor adjustments. A 100 mL Erlenmeyer flask equipped with a magnetic stirring bar was filled with acetylacetone (1 eq.) in anhydrous diethyl ether and chilled in an ice/NaCl bath to 0 °C. The sulfuryl chloride (1 eq.) was added gradually to the conical flask using the dropping funnel such that the internal temperature was kept below 5 °C. In the next step, the reaction mixture was stirred for 2 hours, the solvent was extracted under reduced pressure, and the mixture was washed with sodium bicarbonate and dried over magnesium sulfate, yielding a crude product suitable for further processing without further purification.

**5.1.3. General procedure for the synthesis of intermediates 5a and 5b.**[56]

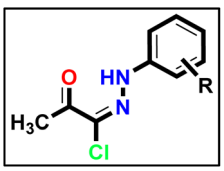

A solution of appropriate aromatic amine (1 eq.), namely (4-methoxyaniline and/or 4-chloroaniline) in concentrated hydrochloric acid (12 M) plus water (200 mL) was stirred in a 500 mL round-bottomed flask for 30 min. Then, the reaction flask was cooled by immersion in ice and salt, until the temperature of the acid reached 0 °C. A solution of sodium nitrite (1.1 eq.) in water (10 mL) was gradually added to the reaction mixture so that the reaction temperature was maintained below 5 °C. This required about 30 minutes under stirring conditions. A separate solution containing sodium acetate (1 eq.) and α-chloro-2,4-pentanedione (2) (1 eq.) in commercially available ethyl alcohol was added in portions. The mixture was then warmed to 25 °C and stirred continuously for 16 h, and the formed precipitate was separated by filtration, rinsed with water, and subsequently dried, resulting in the formation of **5a** and **5b**.

**5.1.4. General procedure for the synthesis of intermediate 9.**

Methyl hydrazinecarbodithioate **9** was synthesized using hydrazine hydrate, carbon disulfide, and methyl iodide, following the same methodology described in a previous publication.[57]

**5.1.5. General procedure for the synthesis of intermediate 12.**

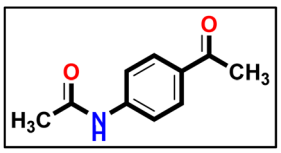

The compound was synthesized using a method described in the literature[58] with a few minor adjustments. An equal amount of triethylamine (1 eq.) was added to a solution of 4-aminoacetophenone (1 eq.) and acetic anhydride (2 eq.) in dimethyl formamide (10 mL), as a reaction solvent. Afterward, the mixture was stirred for 1 hour at ambient temperature. The precipitate which formed was separated and collected on a suction funnel, washed with ice-cold, and dried and purified by recrystallization from ethanol to afford the desired compound (the product was white with yield of 90%).

**5.1.6. General procedure for the synthesis of intermediate 13.**

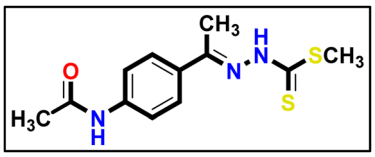

Compound **12** (1 eq.) was solubilized in absolute ethanol (10 mL) and 1 eq. of methyl hydrazinecarbodithioate **9** was added. The reaction mixture was heated under reflux for 7 h (TLC analysis). The obtained solid was filtered while hot, washed with hot ethanol, dried, and recrystallized from dioxane to produce the corresponding compound **13** in 80% yield.

Yellow powder (yield, 73%); m.p. = 255–257 °C. $^1$H NMR (500 MHz, DMSO-$d_6$) δ 12.35 (s, 1H, NH), 10.10 (s, 1H, NH), 7.85–7.73 (m, 2H, Ar–H), 7.66–7.53 (m, 2H, Ar–H), 2.47 (s, 3H, $CH_3$), 2.32 (s, 3H, $CH_3$), 2.03 (s, 3H, $CH_3$); $^{13}$C NMR (101 MHz, DMSO-$d_6$) δ 199.44, 151.45, 141.00, 140.57, 131.58, 127.24, 127.08, 118.53, 24.12, 17.03, 14.43 for $C_{12}H_{15}N_3OS_2$ (281.39).

**5.1.7. General procedure for the synthesis of *N*-(4-((*E*)-1-(((*Z*)-5-acetyl-3-(4-methoxyphenyl)-1,3,4-thiadiazol-2(3*H*)-ylidene)hydrazineylidene)ethyl)phenyl)acetamide 14.**

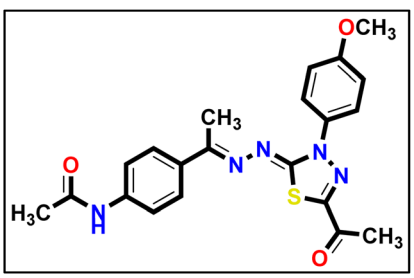

To prepare the derivative **14**, applicable quantities of hydrazonoyl chloride **5a** (1 eq.)

and intermediate **13** (1 eq.) were mixed in absolute ethanol (20 mL). An equivalent amount of triethylamine (1 eq.) was added to the mixture, which was then heated under reflux for 6 hours. The resulting solid was filtered, washed with hot ethanol, and then purified with hexane to obtain the desired final product.

Yellow powder (yield, 70%); m.p. = 283–285 °C. FT-IR ($\nu_{max}$, $cm^{-1}$): 3387, 3305 (NH), 3084, 3007 (C–H aromatic), 2952, 2929 (C–H aliphatic), 1688, 1665 (C=O); $^1$H NMR (400 MHz, DMSO-$d_6$) δ 10.14 (s, 1H, NH), 7.96–7.88 (m, 2H, Ar–H), 7.82 (d, $J$ = 8.5 Hz, 2H, Ar–H), 7.66 (d, $J$ = 8.5 Hz, 2H, Ar–H), 7.17–7.09 (m, 2H, Ar–H), 3.84 (s, 3H, $OCH_3$), 2.57 (s, 3H, $CH_3$), 2.36 (s, 3H, $CH_3$), 2.08 (s, 3H, $CH_3$); $^{13}$C NMR (101 MHz, DMSO-$d_6$) δ 190.13, 169.02, 164.68, 160.01, 158.63, 150.52, 141.32, 132.27, 132.23, 127.52, 124.47, 119.01, 114.66, 55.96, 25.46, 24.56, 15.55; mass (*m/z*): 423 ($M^+$, 5%), 85 (100%, base peak); anal. calcd. for $C_{21}H_{21}N_5O_3S$ (423.49): C, 59.56; H, 5.00; N, 16.54; found: C, 59.84; H, 5.13; N, 16.78%.

**5.1.8. General procedure for the synthesis of intermediates 16a–c.**

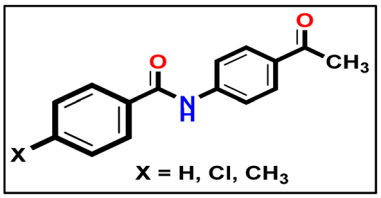


To synthesize intermediates **16a–c**, we followed a process analogous to that used for **12**. We combined derivative **10** (1 eq.) with diverse (un)substituted benzoyl chlorides **15a–c** (1 eq.).

**5.1.9. General procedure for the synthesis of intermediates 17a–c.** Compounds **17a–c** were produced by utilizing 1 eq. of **16a–c** and 1 e of intermediate **9**, following the same method used to synthesize intermediate **13**.

*5.1.9.1. Methyl (E)-2-(1-(4-benzamidophenyl)ethylidene) hydrazine-1-carbodithioate* ***17a.***

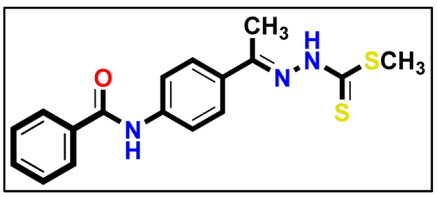


Yellow powder (yield, 80%); m.p. = 250–252 °C. $^1$H NMR (500 MHz, DMSO-$d_6$) δ 12.39 (s, 1H, NH), 10.41 (s, 1H, NH), 8.00–7.92 (m, 3H, Ar–H), 7.84 (m, 3H, Ar–H), 7.58 (m, 1H, Ar–H), 7.52 (d, $J$ = 7.5 Hz, 2H, Ar–H), 2.49 (s, 3H, $CH_3$), 2.35 (s, 3H, $CH_3$); $^{13}$C NMR (101 MHz, DMSO-$d_6$) δ 199.51, 165.99, 151.43, 140.90, 132.18, 131.74, 129.30, 128.42, 127.80, 127.72, 127.10, 119.83, 119.42, 17.01, 14.45 for $C_{17}H_{17}N_3OS_2$ (343.46).

*5.1.9.2. Methyl (E)-2-(1-(4-(4-chlorobenzamido)phenyl) ethylidene)hydrazine-1-carbodi thioate* ***17b.***

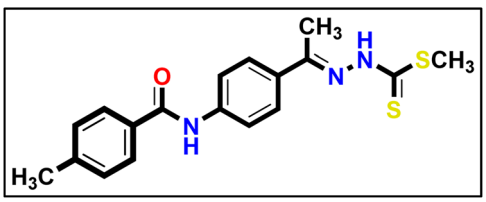


Yellowish white powder (yield, 85%); m.p. = 265–267 °C. $^1$H NMR (500 MHz, DMSO-$d_6$) δ 12.39 (s, 1H, NH), 10.46 (s, 1H, NH), 8.00–7.95 (m, 3H, Ar–H), 7.84 (t, $J$ = 6.2 Hz, 3H, Ar–H), 7.59 (dd, $J$ = 8.3, 4.5 Hz, 2H, Ar–H), 2.52 (s, 3H, $CH_3$), 2.35 (s, 3H, $CH_3$); for $C_{17}H_{16}ClN_3OS_2$ (377.91).

*5.1.9.3. Methyl (E)-2-(1-(4-(4-methylbenzamido)phenyl) ethylidene)hydrazine-1-carbodi thioate* ***17c.***

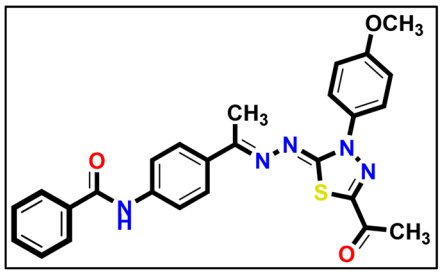


Orange powder (yield, 82%); m.p. = 270–272 °C. $^1$H NMR (500 MHz, DMSO-$d_6$) δ 12.39 (s, 1H), 10.31 (s, 1H), 7.93 (d, $J$ = 5.9 Hz, 1H), 7.87–7.83 (m, 5H), 7.32 (d, $J$ = 7.6 Hz, 2H), 2.52 (s, 3H), 2.36 (s, 3H), 2.35 (s, 3H); $^{13}$C NMR (101 MHz, DMSO-$d_6$) δ 199.58, 165.54, 151.47, 141.85, 141.02, 129.33, 128.98, 127.81, 127.12, 119.84, 119.42, 21.08, 17.05, 14.48 for $C_{18}H_{19}N_3OS_2$ (357.49).

**5.1.10. General procedure for the synthesis of derivatives 18a–f.** Triethylamine (1 equivalent) and the corresponding hydrazonoyl chlorides **5a** and **5b** [specifically, (*E*)-*N*-(4-methoxyphenyl)-2-oxopropanehydrazonoyl chloride (**5a**) and (*E*)-*N*-(4-chlorophenyl)-2-oxopropanehydrazonoyl chloride (**5b**)] (1 equivalent) were combined with a solution of intermediate **17a–c** (1 equivalent) in ethanol (20 mL). The mixture was exposed to heat for a duration of 6 hours. After this period, the resultant solid was gathered and then subjected to purification using hexane to obtain the desired final products.

*5.1.10.1. N-(4-((E)-1-(((Z)-5-Acetyl-3-(4-methoxyphenyl)-1,3,4-thiadiazol-2(3H)-ylidene) hydrazono)ethyl)phenyl) benzamide* ***18a.***

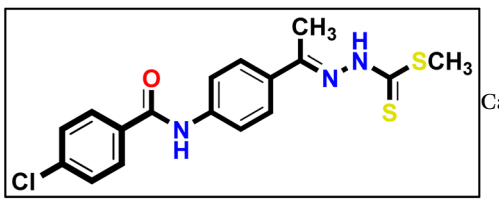


Canary yellow powder (yield, 78%); m.p. = 258–260 °C. FT-IR ($\nu_{max}$, $cm^{-1}$): 3285 (NH), 3058, 3010 (C–H aromatic), 2923, 2834 (C–H aliphatic), 1686, 1654 (C=O); $^1$H NMR (400 MHz, DMSO-$d_6$) δ 10.46 (s, 1H, NH), 8.02–7.98 (m, 3H, Ar–H), 7.91 (m, 5H, Ar–H), 7.63–7.60 (m, 1H, Ar–H), 7.58–7.55 (m, 2H, Ar–H), 7.18–7.12 (m, 2H, Ar–H), 3.85 (s, 3H, $CH_3$), 2.59 (s, 3H, $CH_3$), 2.41 (s, 3H, $CH_3$); $^{13}$C NMR (101 MHz, DMSO-$d_6$) δ 190.14, 166.16, 164.80, 160.04, 158.65, 150.56, 141.24, 135.25, 132.88, 132.23, 132.20, 128.91, 128.25, 128.22, 128.02, 127.40, 124.52, 120.32, 114.68, 55.96, 25.48, 15.61; mass (*m/z*): 485 ($M^+$, 6.72%), 66 (100%, base peak); anal. calcd. for $C_{26}H_{23}N_5O_3S$ (485.56): C, 64.31; H, 4.77; N, 14.42; found: C, 64.19; H, 4.89; N, 14.70%.

*5.1.10.2. N-(4-((E)-1-(((Z)-5-Acetyl-3-(4-chlorophenyl)-1,3,4-thiadiazol-2(3H)-ylidene) hydrazono)ethyl)phenyl) benzamide* ***18b.***

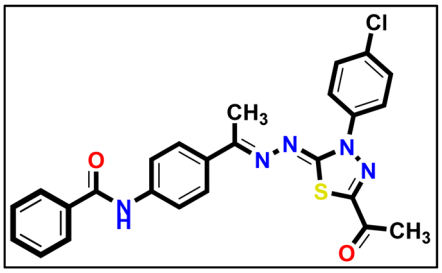

Yellow powder (yield, 72%); m.p. = 267–269 °C. FT-IR ($\nu_{max}$, $cm^{-1}$): 3331, 3103 (NH), 3067, 3014 (C–H aromatic), 1682, 1654 (C=O);$^1$H NMR (400 MHz, DMSO-$d_6$) δ 10.46 (s, 1H), 8.14 (d, $J$ = 8.5 Hz, 2H, Ar–H), 7.96 (m, 6H, Ar–H), 7.73–7.50 (m, 5H, Ar–H), 2.61 (s, 3H, $CH_3$), 2.44 (s, 3H, $CH_3$); $^{13}$C NMR (101 MHz, DMSO-$d_6$) δ 190.24, 166.17, 164.32, 160.79, 151.46, 141.40, 138.14, 135.25, 132.68, 132.21, 131.48, 129.59, 128.90, 128.23, 127.52, 123.82, 120.30, 25.53, 15.81; mass (*m/z*): 489 ($M^+$, 27.03%), 77 (100%, base peak); anal. calcd. for $C_{25}H_{20}ClN_5O_2S$ (489.98): C, 61.28; H, 4.11; N, 14.29; found: C, 61.44; H, 4.29; N, 14.57%.

*5.1.10.3. N-(4-((E)-1-(((Z)-5-Acetyl-3-(4-methoxyphenyl)-1,3,4-thiadiazol-2(3H)-ylidene) hydrazono)ethyl)phenyl)-4-chlorobenzamide* ***18c.***

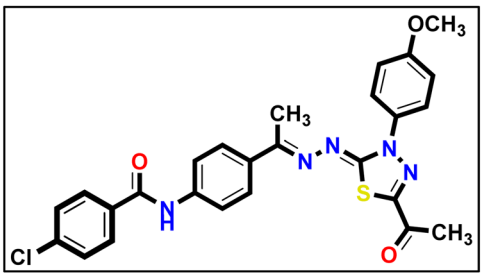

Yellow powder (yield, 80%); m.p. = 245–247 °C. FT-IR ($\nu_{max}$, $cm^{-1}$): 3248, 3105 (NH), 3003 (C–H aromatic), 2931, 2838 (C–H aliphatic), 1691, 1643 (C=O); $^1$H NMR (400 MHz, DMSO-$d_6$) δ 10.50 (s, 1H, NH), 8.06–7.99 (m, 2H, Ar–H), 8.00–7.84 (m, 6H, Ar–H), 7.68–7.60 (m, 2H, Ar–H), 7.19–7.10 (m, 2H, Ar–H), 3.85 (s, 3H, $CH_3$), 2.58 (s, 3H, $CH_3$), 2.40 (s, 3H, $CH_3$); $^{13}$C NMR (101 MHz, DMSO-$d_6$) δ 190.13, 165.02, 164.83, 160.00, 158.65, 150.57, 141.02, 137.03, 133.93, 133.04, 132.23, 130.19, 128.97, 127.41, 124.50, 120.38, 114.68, 55.96, 25.47, 15.60; mass (*m/z*): 520 ($M^+$, 34.8%), 294 (100%, base peak); anal. calcd. for $C_{26}H_{22}ClN_5O_3S$ (520.00): C, 60.05; H, 4.26; N, 13.47; found: C, 60.26; H, 4.41; N, 13.73%.

*5.1.10.4. N-(4-((E)-1-(((Z)-5-Acetyl-3-(4-chlorophenyl)-1,3,4-thiadiazol-2(3H)-ylidene) hydrazono) ethyl)phenyl)-4-chlorobenzamide* ***18d.***

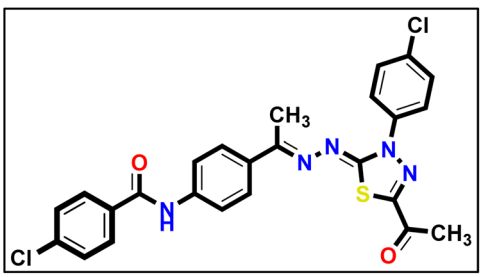

Yellow powder (yield, 75%); m.p. = 275–277 °C. FT-IR ($\nu_{max}$, $cm^{-1}$): 3411 (NH), 3098 (C–H aromatic), 2923 (C–H aliphatic), 1689, 1659 (C=O); $^1$H NMR (400 MHz, DMSO-$d_6$) δ 10.52 (s, 1H, NH), 8.21–8.12 (m, 2H, Ar–H), 8.07–8.00 (m, 2H, Ar–H), 7.95–7.86 (m, 4H, Ar–H), 7.73–7.60 (m, 4H, Ar–H), 2.62 (s, 3H, $CH_3$), 2.46 (s, 3H, $CH_3$); $^{13}$C NMR (101 MHz, DMSO-$d_6$) δ 190.28, 165.05, 160.81, 151.50, 141.19, 138.14, 137.05, 131.54, 130.21, 129.62, 128.99, 127.56, 123.94, 120.41, 15.83. Mass (*m/z*): 524 ($M^+$, 25.53%), 264 (100%, base peak); anal. calcd. for $C_{25}H_{19}Cl_2N_5O_2S$ (524.42): C, 57.26; H, 3.65; N, 13.35; found: C, 57.53; H, 3.91; N, 13.61%.

*5.1.10.5. N-(4-((E)-1-(((Z)-5-Acetyl-3-(4-methoxyphenyl)-1,3,4-thiadiazol-2(3H)-ylidene) hydrazono) ethyl)phenyl)-4-methylbenzamide* ***18e.***

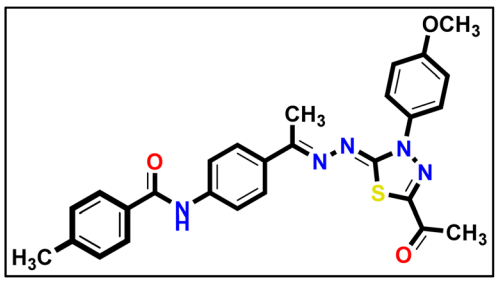

Mustard yellow powder (yield, 80%); m.p. = 240–242 °C. FT-IR ($\nu_{max}$, $cm^{-1}$): 3290 (NH), 3086, 3063, 3006 (C–H aromatic), 2962, 2930, 2835 (C–H aliphatic), 1684, 1643 (C=O); $^1$H NMR (400 MHz, DMSO-$d_6$) δ 10.36 (s, 1H, NH), 7.95–7.87 (m, 8H, Ar–H), 7.37 (d, $J$ = 7.9 Hz, 2H, Ar–H), 7.17–7.12 (m, 2H, Ar–H), 3.85 (s, 3H, $CH_3$), 2.59 (s, 3H, $CH_3$), 2.40 (s, 3H, $CH_3$), 2.41 (s, 3H, $CH_3$); $^{13}$C NMR (101 MHz, DMSO-$d_6$) δ 190.14, 165.94, 164.75, 160.07, 158.66, 150.56, 142.25, 141.33, 132.76, 132.35, 132.24, 129.42, 128.26, 127.38, 124.52, 120.30, 114.68, 55.97, 25.48, 21.52, 15.61; mass (*m/z*): 499 ($M^+$, 16.1%), 158 (100%, base peak); anal. calcd. for $C_{27}H_{25}N_5O_3S$ (499.59): C, 64.91; H, 5.04; N, 14.02; found: C, 64.79; H, 5.23; N, 14.29%.

*5.1.10.6. N-(4-((E)-1-(((Z)-5-Acetyl-3-(4-chlorophenyl)-1,3,4-thiadiazol-2(3H)-ylidene) hydrazono) ethyl)phenyl)-4-methylbenzamide* ***18f.***

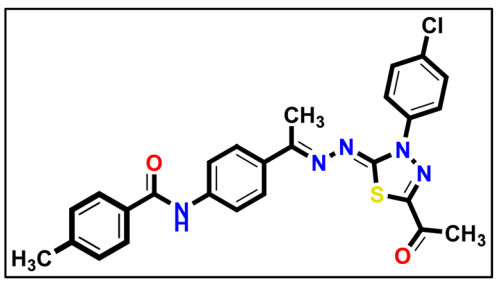

Pale yellow powder (yield, 77%); m.p. = 235–237 °C. FT-IR ($\nu_{max}$, $cm^{-1}$): 3328, 3100 (NH), 3066, 3012 (C–H aromatic), 2917 (C–H aliphatic), 1692, 1651 (C=O); $^1$H NMR (400 MHz, DMSO-$d_6$) δ 8.20–8.12 (m, 2H), 7.92 (m, 7H, Ar–H), 7.73–7.64 (m, 2H, Ar–H), 7.37 (d, $J$ = 8.0 Hz, 2H, Ar–H), 2.63 (s, 3H, $CH_3$), 2.46 (s, 3H, $CH_3$), 2.41 (s, 3H, $CH_3$); $^{13}$C NMR (126 MHz, DMSO-$d_6$) δ 166.03, 164.16, 161.00, 151.49, 142.23, 141.53, 138.27, 132.51, 131.64, 129.59, 129.41, 128.26, 127.51, 123.99, 120.47, 25.50, 21.49, 15.82; mass (*m/z*): 504 ($M^+$, 7.55%), 301 (100%, base peak); anal. calcd. for $C_{26}H_{22}ClN_5O_2S$ (504.01): C, 61.96; H, 4.40; N, 13.90. found: C, 61.82; H, 4.62; N, 14.17%.

### 5.2. Biological evaluation

**5.2.1. *In vitro* anti-proliferative activity.** The synthesized derivatives were examined for their anti-proliferation impact against MCF-7 and HepG2 cancer cell lines *via* the MTT assay[64–66] as presented in the ESI.†

**5.2.2. *In vitro* cytotoxicity against normal human lung cells.** Cytotoxic activity of the most active anti-proliferative analogue **14** was evaluated against normal human lung cells (WI-38) using the MTT assay technique,[67] as shown in the ESI.†

**5.2.3. *In vitro* VEGFR-2 inhibition.** The most active anti-proliferative analogue **14** was tested against VEGFR-2 using a VEGFR-2 ELISA kit,[68] as described in the ESI.†

**5.2.4. *In vitro* DNA-flow cytometric (cell cycle) analysis.** To investigate the impact of compound **14** on the various stages of the MCF-7 cell cycle, cell cycle flow cytometry analysis was performed, as shown in the ESI.†,[67,69].

**5.2.5. Apoptosis analysis.** An annexin V-FITC-apoptosis detection kit was used to investigate the apoptotic effect of compound **14** on the MCF-7 treated cells with the aid of ab Epics XL-MCL™ Flow Cytometer [33,41], as detailed in the ESI.†

**5.2.6. Assessment of Bcl-2 and BAX expression.** The Bcl-2 and BAX expression levels were estimated according to the reported procedure and described in detail in the ESI.†

**5.2.7. Cell migration assay.** Cell migration assay was performed in MCF-7 treated cells as presented in the ESI.†,[61]

### 5.3. *In silico* studies

**5.3.1. DFT analysis.** DFT computations were performed utilizing Gaussian09W.01D software at the B3LYP/6-311G++(d,p) level of theory. For the evaluation of the reactivity indices, electrostatic surface potential (ESP), and total electron density of states (TDOS) of compound **14**, GaussView5 and GaussSum 3.0 programs were employed. These computational resources played a crucial role in acquiring insightful data on the reactivity and electronic attributes of compound **14**, thereby enriching the scope of our study.[70]

**5.3.2. Docking studies.** Docking was performed for the thiadiazole derivatives against the VEGFR-2 protein by MOE2014 software.[71] For a more comprehensive understanding and detailed analysis, please refer to the ESI.†

**5.3.3. MD simulation studies.** A 200 nanosecond classical molecular dynamics (MD) simulation was performed using GROMACS 2021 to evaluate the stability of the VEGFR-2–compound **22** complex and to analyze the interactions and differences between the holo and apo structures. The input files were created using the solution builder module of the CHARMM-GUI web server.[72] For a more comprehensive understanding and detailed analysis, please refer to the ESI.†

**5.3.4. MM-GBSA.** The binding affinity was evaluated using the molecular mechanics-generalized born surface area (MM-GBSA) approach, implemented through the gmx_MMPBSA program.[73] For a more comprehensive understanding and detailed analysis, please refer to the ESI.†

**5.3.5. PCAT and FEL analysis.** Principal component analysis (PCA) was conducted on the mass-weighted covariance matrix (C) of a specified subset of atoms. This analysis specifically targeted the alpha carbons of amino acids spanning from Glu826 to Leu1161, excluding the terminal amino acids. The objective was to examine the collective motion observed in molecular dynamics (MD) trajectories.[74] In order to compare the two trajectories, we generated plots based on the projection onto the first three eigenvectors, utilizing various combinations of these eigenvectors.[75] For a more comprehensive understanding and detailed analysis, please refer to the ESI.†

**5.3.6. ADMET and toxicity studies.** ADMET profiles were predicted for the thiadiazole derivatives and sorafenib by Discovery Studio 4.0.[76,77] For a more comprehensive understanding and detailed analysis, please refer to the ESI.†

## Conflicts of interest

None.

## Acknowledgements

This research was funded by Princess Nourah Bint Abdulrahman University Researchers Supporting Project number (PNURSP2023R116), Princess Nourah bint Abdulrahman University, Riyadh, Saudi Arabia. The authors extend their appreciation to the Research Center at AlMaarefa University for funding this work.

## References

1 International Agency for Research on Cancer, *Cancer-Population Fact Sheets*, **https://gco.iarc.fr/today/data/factsheets/populations/900-world-fact-sheets.pdf**, (accessed 10-10-2023, 2023).
2 J.-D. Yan, Y. Liu, Z.-Y. Zhang, G.-Y. Liu, J.-H. Xu, L.-Y. Liu and Y.-M. Hu, *Pathol., Res. Pract.*, 2015, **211**, 539–543.
3 J. Bai, J. Wu, R. Tang, C. Sun, J. Ji, Z. Yin, G. Ma and W. Yang, *Invest. New Drugs*, 2020, **38**, 229–245.
4 X. Wang, A. M. Bove, G. Simone and B. Ma, *Front. Cell Dev. Biol.*, 2020, **8**, 599281.
5 R. Lugano, M. Ramachandran and A. Dimberg, *Cell. Mol. Life Sci.*, 2020, **77**, 1745–1770.
6 N. Fathi Maroufi, S. Taefehshokr, M.-R. Rashidi, N. Taefehshokr, M. Khoshakhlagh, A. Isazadeh, N. Mokarizadeh, B. Baradaran and M. Nouri, *Mol. Biol. Rep.*, 2020, **47**, 4749–4765.
7 A. A. Shah, M. A. Kamal and S. Akhtar, *Curr. Drug Metab.*, 2021, **22**, 50–59.
8 W. A. Spannuth, A. M. Nick, N. B. Jennings, G. N. Armaiz-Pena, L. S. Mangala, C. G. Danes, Y. G. Lin, W. M. Merritt, P. H. Thaker and A. A. Kamat, *Int. J. Cancer*, 2009, **124**, 1045–1053.
9 F. W. Peng, D. K. Liu, Q. W. Zhang, Y. G. Xu and L. Shi, *Expert Opin. Ther. Pat.*, 2017, **27**, 987–1004.
10 X. Li, J. Chai, Z. Wang, L. Lu, Q. Zhao, J. Zhou and F. Ju, *OncoTargets Ther.*, 2018, **11**, 4407–4411.
11 P. Tesařová and V. Tesař, *Folia Biol.*, 2013, **59**, 15–25.
12 C. Fontanella, E. Ongaro, S. Bolzonello, M. Guardascione, G. Fasola and G. Aprile, *Ann. Transl. Med.*, 2014, **2**, 123.

13 L. Erdem, E. Giovannetti, L. G. Leon, R. Honeywell and G. J. Peters, *Curr. Top. Med. Chem.*, 2012, **12**, 1649–1659.
14 A. Levy, L. Benmoussa, S. Ammari, L. Albiges and B. Escudier, *Clin. Genitourin. Cancer*, 2014, **12**, e33–e34.
15 S. Grimme and P. R. Schreiner, *Angew. Chem., Int. Ed. Engl.*, 2018, **57**, 4170–4176.
16 D. Reker and G. J. D. d. t, *Schneider*, 2015, **20**, 458–465.
17 X. Yang, Y. Wang, R. Byrne, G. Schneider and S. Yang, *Chem. Rev.*, 2019, **119**, 10520–10594.
18 H. González-Díaz, *Curr. Top. Med. Chem.*, 2021, **21**, 789.
19 H. Willems, S. De Cesco and F. Svensson, *J. Med. Chem.*, 2020, **63**, 10158–10169.
20 B. De, K. Bhandari, F. J. B. Mendonça, M. T. Scotti and L. Scotti, *Anti-Cancer Agents Med. Chem.*, 2019, **19**, 587–591.
21 G. D. Geromichalos, *J. B.U.ON.*, 2007, **12**(Suppl 1), S101–S118.
22 R. Hameed, A. Khan, S. Khan and S. Perveen, *Anti-Cancer Agents Med. Chem.*, 2019, **19**, 592–598.
23 G. D. Geromichalos, C. E. Alifieris, E. G. Geromichalou and D. T. Trafalis, *J. B.U.ON.*, 2016, **21**, 1337–1358.
24 D. C. Elton, Z. Boukouvalas, M. D. Fuge and P. W. Chung, *Mol. Syst. Des. Eng.*, 2019, **4**, 828–849.
25 J. Fan, A. Fu and L. Zhang, *Quant. Biol.*, 2019, **7**, 83–89.
26 L. L. Ferreira and A. D. Andricopulo, *Drug discovery today*, 2019, **24**, 1157–1165.
27 I. Obot, D. Macdonald and Z. Gasem, *Corros. Sci.*, 2015, **99**, 1–30.
28 N. del Carmen Quintal Bojórquez and M. R. Campos, *Curr. Cancer Drug Targets*, 2023, **23**, 333–345.
29 Q. B. NDC and M. Campos, *Curr. Cancer Drug Targets*, 2022, **23**(5), 333–345.
30 O. Daoui, S. N. Mali, K. Elkhattabi, S. Elkhattabi and S. Chtita, *Heliyon*, 2023, **9**, e15545.
31 I. J. d. S. Nascimento, T. M. de Aquino and E. F. da Silva-Júnior, *Lett. Drug Des. Discovery*, 2022, **19**, 951–955.
32 M. S. Taghour, H. Elkady, W. M. Eldehna, N. El-Deeb, A. M. Kenawy, A. E. Abd El-Wahab, E. B. Elkaeed, B. A. Alsfouk, A. M. Metwaly and I. H. Eissa, *J. Biomol. Struct. Dyn.*, 2022, 1–16.
33 E. B. Elkaeed, M. S. Taghour, H. A. Mahdy, W. M. Eldehna, N. M. El-Deeb, A. M. Kenawy, B. A. Alsfouk, M. A. Dahab, A. M. Metwaly and I. H. Eissa, *J. Enzyme Inhib. Med. Chem.*, 2022, **37**, 2191–2205.
34 I. H. Eissa, R. G. Yousef, H. Elkady, E. B. Elkaeed, A. A. Alsfouk, D. Z. Husein, I. M. Ibrahim, M. A. Elhendawy, M. Godfrey and A. M. Metwaly, *Comput. Biol. Chem.*, 2023, **107**, 107953.
35 I. H. Eissa, R. G. Yousef, H. Elkady, E. B. Elkaeed, A. A. Alsfouk, D. Z. Husein, I. M. Ibrahim, M. M. Radwan and A. M. Metwaly, *ChemistryOpen*, 2023, **12**, e202300066.
36 H. A. Mahdy, H. Elkady, M. S. Taghour, A. Elwan, M. A. Dahab, M. A. Elkady, E. G. Elsakka, E. B. Elkaeed, B. A. Alsfouk, I. M. Ibrahim, I. H. Eissa and A. M. Metwaly, *Future Med. Chem.*, 2023, **15**, 1233–1250.
37 M. A. Dahab, H. A. Mahdy, H. Elkady, M. S. Taghour, A. Elwan, M. A. Elkady, E. G. E. Elsakka, E. B. Elkaeed, A. A. Alsfouk, I. M. Ibrahim, A. M. Metwaly and I. H. Eissa, *J. Biomol. Struct. Dyn.*, 2023, 1–20, DOI: 10.1080/07391102.2023.2219333.
38 I. H. Eissa, R. G. Yousef, H. Elkady, E. B. Elkaeed, B. A. Alsfouk, D. Z. Husein, M. A. Asmaey, I. M. Ibrahim and A. M. Metwaly, *Pathol., Res. Pract.*, 2023, **251**, 154894.
39 A. Elwan, A. E. Abdallah, H. A. Mahdy, M. A. Dahab, M. S. Taghour, E. B. Elkaeed, A. B. Mehany, A. Nabeeh, M. Adel and A. A. Alsfouk, *Molecules*, 2022, **27**, 5047.
40 M. S. Taghour, H. A. Mahdy, M. H. Gomaa, A. Aglan, M. G. Eldeib, A. Elwan, M. A. Dahab, E. B. Elkaeed, A. A. Alsfouk and M. M. Khalifa, *J. Enzyme Inhib. Med. Chem.*, 2022, **37**, 2063–2077.
41 E. B. Elkaeed, R. G. Yousef, H. Elkady, I. M. Gobaara, B. A. Alsfouk, D. Z. Husein, I. M. Ibrahim, A. M. Metwaly and I. H. Eissa, *Molecules*, 2022, **27**, 4606.
42 R. G. Yousef, A. Elwan, I. M. Gobaara, A. B. Mehany, W. M. Eldehna, S. A. El-Metwally, B. A. Alsfouk, E. B. Elkaeed, A. M. Metwaly and I. H. Eissa, *J. Enzyme Inhib. Med. Chem.*, 2022, **37**, 2206–2222.
43 H. Elkady, A. A. Abuelkhir, M. Rashed, M. S. Taghour, M. A. Dahab, H. A. Mahdy, A. Elwan, H. A. Al-Ghulikah, E. B. Elkaeed, I. M. Ibrahim, D. Z. Husein, A. Metwaly and I. H. Eissa, *Comput. Biol. Chem.*, 2023, **107**, 107958.
44 R. G. Yousef, H. Elkady, E. B. Elkaeed, I. M. Gobaara, H. A. Al-Ghulikah, D. Z. Husein, I. M. Ibrahim, A. M. Metwaly and I. H. Eissa, *Molecules*, 2022, **27**, 7719.
45 E. B. Elkaeed, R. G. Yousef, H. Elkady, A. B. Mehany, B. A. Alsfouk, D. Z. Husein, I. M. Ibrahim, A. M. Metwaly and I. H. Eissa, *J. Biomol. Struct. Dyn.*, 2022, 1–16.
46 M. A. El-Zahabi, H. Elkady, H. Sakr, A. S. Abdelraheem, S. I. Eissa and K. El-Adl, *J. Biomol. Struct. Dyn.*, 2023, 1–18.
47 M. M. Alanazi, H. A. Mahdy, N. A. Alsaif, A. J. Obaidullah, H. M. Alkahtani, A. A. Al-Mehizia, S. M. Alsubaie, M. A. Dahab and I. H. Eissa, *Bioorg. Chem.*, 2021, **112**, 104949.
48 M. M. Alanazi, H. Elkady, N. A. Alsaif, A. J. Obaidullah, H. M. Alkahtani, M. M. Alanazi, M. A. Alharbi, I. H. Eissa and M. A. Dahab, *RSC Adv.*, 2021, **11**, 30315–30328.
49 R. G. Yousef, H. M. Sakr, I. H. Eissa, A. B. Mehany, A. M. Metwaly, M. A. Elhendawy, M. M. Radwan, M. A. ElSohly, H. S. Abulkhair and K. El-Adl, *New J. Chem.*, 2021, **45**, 16949–16964.
50 L. Adnane, P. A. Trail, I. Taylor and S. M. Wilhelm, *Methods Enzymol.*, 2006, **407**, 597–612.
51 F.-W. Peng, D.-K. Liu, Q.-W. Zhang, Y.-G. Xu and L. Shi, *Expert Opin. Ther. Pat.*, 2017, **27**, 987–1004.
52 M. G. Papich, *Papich Handbook of Veterinary Drugs-E-Book*, Elsevier Health Sciences, 2020.
53 G. J. Roth, R. Binder, F. Colbatzky, C. Dallinger, R. Schlenker-Herceg, F. Hilberg, S.-L. Wollin and R. Kaiser, *J. Med. Chem.*, 2015, **58**, 1053–1063.
54 H. Elkady, O. A. El-Dardir, A. Elwan, M. S. Taghour, H. A. Mahdy, M. A. Dahab, E. B. Elkaeed, B. A. Alsfouk, I. M. Ibrahim and D. Z. Husein, *RSC Adv.*, 2023, **13**, 27801–27827.
55 R. Verhé, L. De Buyck, N. De Kimpe, A. De Rooze and N. Schamp, *Bull. Soc. Chim. Belg.*, 1978, **87**, 143–152.

56 S. R. Donohue, R. F. Dannals, C. Halldin and V. W. Pike, *J. Med. Chem.*, 2011, **54**, 2961–2970.
57 D. L. Klayman, J. F. Bartosevich, T. S. Griffin, C. J. Mason and J. P. Scovill, *J. Med. Chem.*, 1979, **22**, 855–862.
58 L. Yurttaş, Y. Özkay, G. Akalın-Çiftçi and Ş. Ulusoylar-Yıldırım, *J. Enzyme Inhib. Med. Chem.*, 2014, **29**, 175–184.
59 J. S. Chu, F. J. Ge, B. Zhang, Y. Wang, N. Silvestris, L. J. Liu, C. H. Zhao, L. Lin, A. E. Brunetti and Y. L. Fu, *J. Exp. Clin. Cancer Res.*, 2013, **32**, 1–8.
60 J. Pijuan, C. Barceló, D. F. Moreno, O. Maiques, P. Sisó, R. M. Marti, A. Macià and A. Panosa, *Front. Cell Dev. Biol.*, 2019, **7**, 107.
61 I. Arranz-Valsero, L. Soriano-Romaní, L. García-Posadas, A. López-García and Y. Diebold, *Exp. Eye Res.*, 2014, **125**, 183–192.
62 D. Z. Husein, R. Hassanien and M. Khamis, *RSC Adv.*, 2021, **11**, 27027–27041.
63 T. Wang and D. Z. Husein, *Environ. Sci. Pollut. Res.*, 2023, **30**, 8928–8955.
64 T. Mosmann, *J. Immunol. Methods*, 1983, **65**, 55–63.
65 F. Denizot and R. Lang, *J. Immunol. Methods*, 1986, **89**, 271–277.
66 M. Thabrew, R. D. HUGHES and I. G. MCFARLANE, *J. Pharm. Pharmacol.*, 1997, **49**, 1132–1135.
67 N. A. Alsaif, M. S. Taghour, M. M. Alanazi, A. J. Obaidullah, W. A. Alanazi, A. Alasmari, H. Albassam, M. A. Dahab and H. A. Mahdy, *Bioorg. Med. Chem.*, 2021, **46**, 116384.
68 H. A. Mahdy, H. Elkady, M. S. Taghour, A. Elwan, M. A. Dahab, M. A. Elkady, E. G. Elsakka, E. B. Elkaeed, B. A. Alsfouk and I. M. Ibrahim, *Future Med. Chem.*, 2023, **15**, 1233–1250.
69 A. A. Nasser, I. H. Eissa, M. R. Oun, M. A. El-Zahabi, M. S. Taghour, A. Belal, A. M. Saleh, A. B. Mehany, H. Luesch and A. E. Mostafa, *Org. Biomol. Chem.*, 2020, **18**, 7608–7634.
70 D. Z. Husein, R. Hassanien and M. J. R. A. Khamis, *RSC adv.*, 2021, **11**, 27027–27041.
71 Y. M. Suleimen, R. A. Jose, G. K. Mamytbekova, R. N. Suleimen, M. Y. Ishmuratova, W. Dehaen, B. A. Alsfouk, E. B. Elkaeed, I. H. Eissa and A. M. Metwaly, *Plants*, 2022, **11**, 2072.
72 M. J. Abraham, T. Murtola, R. Schulz, S. Páll, J. C. Smith, B. Hess and E. Lindahl, *SoftwareX*, 2015, **1**, 19–25.
73 M. S. Valdés-Tresanco, M. E. Valdés-Tresanco, P. A. Valiente and E. Moreno, *J. Chem. Theory Comput.*, 2021, **17**, 6281–6291.
74 A. Amadei, A. B. Linssen and H. J. J. P. S. Berendsen, *Funct., Bioinf.*, 1993, **17**, 412–425.
75 E. Papaleo, P. Mereghetti, P. Fantucci, R. Grandori and L. De Gioia, *J. Mol. Graphics Modell.*, 2009, **27**, 889–899.
76 D. S. Biovia, *Release*, 2017.
77 A. M. Metwaly, E. B. Elkaeed, B. A. Alsfouk, A. M. Saleh, A. E. Mostafa and I. H. Eissa, *Plants*, 2022, **11**, 1886–1905.